

**Search for  $E/\nu$  Decay to  $\eta\pi\pi$   
in Proton-Antiproton Annihilation at Rest**

Inaugural Dissertation

zur Erlangung der philosophischen Doktorwürde

vorgelegt der

Philosophischen Fakultät II

der

Universität Zürich

von

David Urner

aus Zürich

begutachtet von Prof. Dr. Claude Amsler

Zürich 1995

# Contents

<b>Zusammenfassung</b>	<b>iii</b>
<b>Abstract</b>	<b>iv</b>
<b>1 Motivation</b>	<b>1</b>
1.1 Introduction . . . . .	1
1.2 SU(3) Classification . . . . .	2
1.3 The E/ $\iota$ Resonance at 1400 MeV . . . . .	4
<b>2 Experiment</b>	<b>7</b>
2.1 Apparatus . . . . .	7
2.1.1 Target . . . . .	8
2.1.2 Multiwire Proportional Chamber (PWC) . . . . .	9
2.1.3 Jet Drift Chamber (JDC) . . . . .	12
2.1.4 Crystal Calorimeter . . . . .	12
2.2 Trigger . . . . .	13
2.2.1 Hardware Trigger . . . . .	13
2.2.2 Software Trigger . . . . .	15
2.2.3 Trigger on the $\pi^+\pi^-\pi^0\pi^0\eta$ Final State . . . . .	16
<b>3 Analysis Method</b>	<b>21</b>
3.1 Calibration . . . . .	21
3.2 Event Reconstruction . . . . .	22
3.3 Monte Carlo Simulation . . . . .	24
3.4 Performance of the Trigger . . . . .	24
3.4.1 1. Trigger Level (Hardware) . . . . .	24
3.4.2 2. Trigger Level (Hardware) . . . . .	26
3.4.3 Software Trigger . . . . .	28

<b>4</b>	<b>The <math>\pi^+\pi^-\pi^0\pi^0\eta</math> Final State</b>	<b>31</b>
4.1	Data Reduction . . . . .	31
4.2	The Final States $\omega\eta\pi^0$ and $\eta\eta\pi^0$ . . . . .	37
4.3	The $\eta\pi\pi$ Invariant Mass Distribution . . . . .	38
4.4	Final State Branching Ratios . . . . .	39
4.5	The $\pi^+\pi^-\pi^0\eta\eta$ Final State . . . . .	42
<b>5</b>	<b>Discussion</b>	<b>45</b>
5.1	Spin-Parity Analysis . . . . .	45
5.1.1	Transition Probability . . . . .	45
5.1.2	Maximum Likelihood Fit . . . . .	47
5.1.3	Overview about Resonances and Decay Chains . . . . .	49
5.2	Results . . . . .	51
5.2.1	General Features . . . . .	51
5.2.2	$E/\iota$ Fit . . . . .	51
5.2.3	$E/\iota$ Mass and Width . . . . .	58
5.2.4	Branching Ratios . . . . .	59
5.3	Conclusion and outlook . . . . .	61
	<b>Bibliography</b>	<b>63</b>
	<b>Acknowledgements</b>	<b>65</b>

# Zusammenfassung

Im Rahmen dieser Arbeit wird die Messung und die Analyse des  $\pi^+\pi^-(\pi^0\pi^0\eta \rightarrow 6\gamma)$  Endzustandes der  $\bar{p}p$  Annihilation in Ruhe beschrieben, mit dem Ziel das E-Meson nachzuweisen und seinen Zerfall nach  $\eta\pi\pi$  zu studieren.

Das E Meson wurde bereits früher in  $\bar{p}p$  annihilation in Ruhe beobachtet (600 Ereignisse im Zerfallskanal  $E \rightarrow K\bar{K}\pi$ ). Die vorliegende Arbeit, durchgeführt mit dem Crystal Barrel Detektor am LEAR/CERN, hat mit etwa 10'000 E Ereignissen den Zerfallskanal  $E \rightarrow \eta\pi\pi$  erstmals nachgewiesen. Der dafür erforderliche Datensatz von 300'000 rekonstruierbaren  $\pi^+\pi^-\pi^0\pi^0\eta$  Ereignissen wurde mit Hilfe eines raffinierten Triggers (mit einer Anreicherung gegenüber ungetriggerten Daten von 100) während 10 Tagen Strahlzeit gemessen. Es wurde bestimmt, dass der Endzustand  $\pi^+\pi^-\pi^0\pi^0\eta$  mit  $(2.08 \pm 0.34)\%$  zur  $\bar{p}p$  Annihilation beiträgt. Ein Bruchteil (ca 7%) der  $\pi^+\pi^-\pi^0\pi^0\eta$  Ereignisse sind vom Typ  $\bar{p}p \rightarrow \pi^+\pi^-(E \rightarrow \eta\pi^0\pi^0)$  oder  $\pi^0\pi^0(E \rightarrow \eta\pi^+\pi^-)$ . Für das absolute Verzweigungsverhältnis wurde folgender Wert bestimmt:

$$B[\bar{p}p \rightarrow \pi\pi(E \rightarrow \eta\pi\pi)] = (1.53 \pm 0.47)10^{-3}. \quad (0.1)$$

Es wurde ein Maximum Likelihood Fit entwickelt, um die Daten mit Hilfe des Helizitätsformalismus im Rahmen des Isobar Modells zu beschreiben. Die  $J^{PC}=0^{-+}$  Hypothese für die Quantenzahlen des E wurde vom Fit der  $1^{++}$  Hypothese klar vorgezogen. Eine Masse von  $1409 \pm 3$  MeV und eine Breite von  $86 \pm 10$  MeV wurden bestimmt. Nimmt man an, dass zwei Resonanzen im Bereich von 1400 MeV existieren, trägt ein zusätzlicher  $1^{++}$  Zustand nur mit  $(5.4 \pm 3.6)\%$  des  $0^{-+}$  Anteils bei.

Dies war die erste Messung, bei der E sowohl nach  $\eta(\pi\pi)_s$  (wo  $(\pi\pi)_s$  ein Dipion in der relativen S-Welle bezeichnet) als auch nach  $a_0\pi$  zerfällt und führt zu folgendem Verhältnis:

$$\frac{B(E \rightarrow (\pi\pi)_s\eta)}{B(E \rightarrow a_0(980)\pi, a_0 \rightarrow \eta\pi)} = 0.73 \pm 0.15. \quad (0.2)$$

Im weiteren impliziert der Zerfall des E nach  $\eta\pi^0\pi^0$ , dass das E positive C-Parität besitzt (und Isospin null), was hier zum ersten Mal direkt gemessen wurde. Benützt man das bekannte Verzweigungsverhältnis für  $\bar{p}p \rightarrow \pi\pi(E \rightarrow K\bar{K}\pi)$ , findet man:  $\frac{a_0 \rightarrow K\bar{K}}{a_0 \rightarrow \eta\pi} = 1.14 \pm 0.31$ .

Somit sind die Quantenzahlen, Masse, Breite und Zerfallsraten für das E Meson konsistent mit denen des  $\iota$ , welches im radiativen  $J/\Psi$  Zerfall nachgewiesen wurde, ein vorzüglicher Kandidat für den  $0^{-+}$  Glueball.

# Abstract

This thesis presents the measurement and analysis of the  $\pi^+\pi^-(\pi^0\pi^0\eta \rightarrow 6\gamma)$  final state in  $\bar{p}p$  annihilation at rest with the goal to find and study the E meson and its decay into  $\eta\pi\pi$ .

The E meson was seen earlier in  $\bar{p}p$  annihilation at rest (600 events in the decay channel  $E \rightarrow K\bar{K}\pi$ ). The present work was done with the Crystal Barrel experiment at LEAR/CERN which found 10'000 E particles decaying into  $\eta\pi\pi$ . For this purpose an elaborated trigger having an enrichment of 100 was set up. In 10 days of beam time 300'000 reconstructed  $\pi^+\pi^-\pi^0\pi^0\eta$  events were collected. It was found that  $(2.08 \pm 0.34)\%$  of the  $\bar{p}p$  atom annihilate into the  $\pi^+\pi^-\pi^0\pi^0\eta$  final state. A fraction ( $\sim 7\%$ ) of the  $\pi^+\pi^-\pi^0\pi^0\eta$  events were found to be  $\bar{p}p \rightarrow \pi^+\pi^-(E \rightarrow \eta\pi^0\pi^0)$  or  $\pi^0\pi^0(E \rightarrow \eta\pi^+\pi^-)$ , which leads to an absolute branching ratio of

$$B[\bar{p}p \rightarrow \pi\pi(E \rightarrow \eta\pi\pi)] = (1.53 \pm 0.47)10^{-3}. \quad (0.3)$$

A maximum likelihood fit was performed to describe the data using the helicity formalism in terms of the isobar model. The  $J^{PC}=0^{-+}$  hypothesis for E was clearly favoured over the  $1^{++}$  hypothesis. A mass of  $1409 \pm 3$  MeV and a width of  $86 \pm 10$  MeV were determined. If one assumes two resonances in the 1400 MeV region, a additional  $1^{++}$  state contributes only with  $(5.4 \pm 3.6)\%$  of the  $0^{-+}$  intensity.

This is the first measurement of E decaying into both  $\eta(\pi\pi)_s$  ( $(\pi\pi)_s$  means a dipion in the relative S-wave) and  $a_0\pi$ . One finds the following ratio:

$$\frac{B(E \rightarrow \eta(\pi\pi)_s)}{B(E \rightarrow a_0(980)\pi, a_0 \rightarrow \eta\pi)} = 0.73 \pm 0.15. \quad (0.4)$$

The decay into  $\eta\pi^0\pi^0$  implies that E has positive C-parity (and isospin 0). This is the first direct measurement of the C-parity. Using the known branching ratio for  $\bar{p}p \rightarrow \pi\pi(E \rightarrow K\bar{K}\pi)$  one finds that  $\frac{a_0 \rightarrow K\bar{K}}{a_0 \rightarrow \eta\pi} = 1.14 \pm 0.31$

The quantum numbers, mass, width and decay rates of the E meson are consistent with those of the  $\iota$  found in radiative  $J/\Psi$  decay, a prominent  $0^{-+}$  glueball candidate.

# Chapter 1

## Motivation

### 1.1 Introduction

The investigation of antiproton-proton annihilation at rest leads to a better understanding of the strong interaction in the low energy regime. This is our final goal, and I understand this work as one step on this difficult path.

The  $\bar{p}p$  annihilation process emits  $q\bar{q}$ -pairs and gluons, and is therefore an excellent tool to study light mesons, multi-quark mesons and gluonic hadrons such as glueballs (bound states of two or more gluons) or hybrids ( $q\bar{q}$  states with an excited gluon). These latter states are predicted by Quantum Chromodynamics (QCD), which is however poorly understood at low energy. One has therefore to resort to QCD inspired models to predict the low energy mass spectrum.

The reason for using models is that for reactions with low momentum transfer, the QCD coupling constant becomes large, and a perturbative treatment is therefore impossible. One type of models tries to describe the annihilation process with particle exchange (nucleon and mesons). The other approach is to use the underlying quark structure, which seems natural, because proton antiproton annihilation is a short range process in which the quark cores overlap.

There are advantages if one studies  $\bar{p}p$  annihilation at rest:

The captured antiproton ejects a K-shell electron and forms an antiprotonic hydrogen atom with the principal quantum number  $n \sim 30$ . In liquid hydrogen, due to Stark Mixing, an average of 90% of the  $\bar{p}p$  atoms decay from the S states ( $^1S_0$  and  $^3S_1$ ). In gaseous hydrogen, one has also to include the P states ( $^3P_2$ ,  $^3P_1$ ,  $^3P_0$  and  $^1P_1$ ) [2]. Considering this restricted number of initial states and the conservation laws (J, P and C) one gets a manageable number of possible intermediate resonances. This also helps to compare experimental data with the models.

The detector of the Crystal Barrel experiment allows to fully reconstruct most

of the possible final states, including charged and neutral particles. Previous experiments had no or only a very restricted ability to detect photons, which however occur (e.g. from  $\pi^0$  and  $\eta$  decays) in 90% of the annihilation channels! The Low Energy Antiproton Ring (LEAR) delivers a continuous beam of up to  $10^6$  antiprotons per second in a momentum range of 100-2000 MeV/c. With the Crystal Barrel detector it is therefore possible to collect enough events so that after filtering several  $10^5$  remain to be used in the spin-parity analyses for various final states. The Crystal Barrel detector is also capable to measure  $\bar{p}p$  in flight. This increases the phase space up to 2540 MeV (at the maximum beam momentum of 2000 MeV/c).

This work, a part of the Crystal Barrel research programme, tries to clarify the nature of the  $E/\iota$  meson (section 1.3) which was found around 1400 MeV, and has controversial spin and parity. The measurement of the  $\pi^+\pi^-\pi^0\pi^0\eta$  final state in  $\bar{p}p$  annihilation at rest with high statistics (chapter 2) includes setting up and testing of all trigger components, which was necessary because this was the first measurement performed with an elaborated trigger. An offline trigger simulation (chapter 3) was performed to take into account trigger effects within the Monte Carlo simulation. The Crystal Barrel collaboration has so far concentrated mainly on final states involving only photons. I therefore had to investigate the effects in the detector caused by the charged particles. In order to isolate the  $\pi^+\pi^-\pi^0\pi^0\eta$  final state (chapter 4) a careful data selection and a kinematic fit procedure were used. A spin-parity analysis (chapter 5) was performed using a maximum likelihood fit in order to describe the  $E/\iota \rightarrow \pi\pi\eta$  decay.

## 1.2 SU(3) Classification

In the naive quark model one combines a quark and an antiquark from the three light quarks (u, d, s) to form a  $q\bar{q}$  pair. They group into an octet and a singlet:

$$3 \otimes 3^* = 8 \oplus 1 \quad (1.1)$$

It is impressive how well this model, which does not include gluonic interactions, works. With the spin of  $\frac{1}{2}$  of the quarks and the relative angular momentum L, one gets the states with spin J parity P and C-parity C ( $J^{PC}$ ) and their radial excitations shown in figure 1.1.

One would also expect to find many meson-meson bound states ( $qq\bar{q}\bar{q}$ ), but this does not seem to be true. Using a potential model Weinstein and Isgur [3][4] found for the  $K\bar{K}$  system weakly bound states, for which they proposed the  $a_0(980)$  and the  $f_0(975)$ .

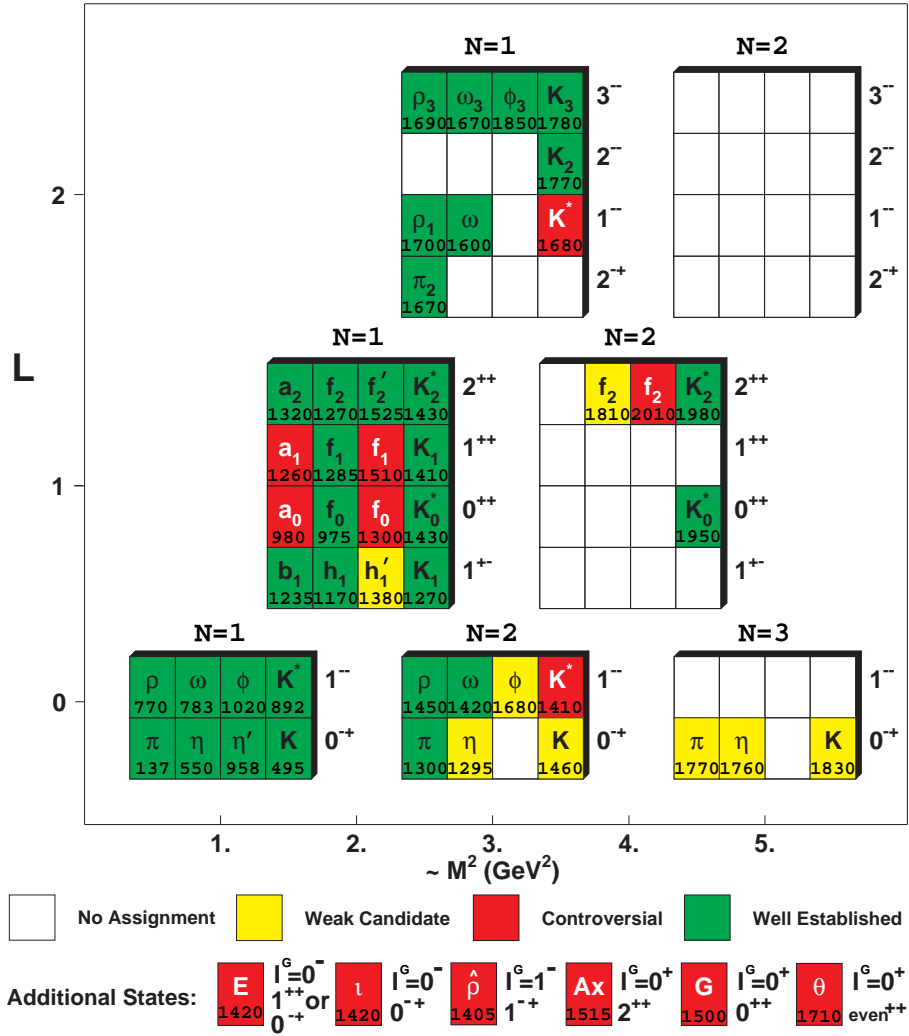


Figure 1.1: Quark model. L is the relative angular momentum. The quadratic mass scale is approximative.

A prediction of QCD are mesons containing exclusively gluons, dubbed glueballs. This is a consequence of gluons coupling strongly to each other. Pure glueballs should decay flavor blind while  $q\bar{q}$  mesons couple more strongly to mesons

with equal flavor contents. It might be difficult to decide whether a certain resonance is a glueball (or maybe a hybrid) since glueball decay rates depart from flavor blindness, due to mixing with nearby  $\bar{q}q$  states [5]. However, the recently discovered  $f_0(1500)$  in the Crystal Barrel (G in fig. 1.1) is a good case [5][6] for the ground state glueball predicted by lattice gauge theories. Models like the MIT bag model or lattice gauge theories are contradictory in their prediction of the mass spectrum and make only rough mass estimations. It is probably necessary to search for the full spectrum of glueballs which would require more energy than twice the proton mass. The Crystal Barrel collaboration is measuring the mass spectrum up to 2400 MeV. For higher energies a new beam facility would be necessary.

### 1.3 The $E/\iota$ Resonance at 1400 MeV

In 1967 the CERN-Collège de France group reported a resonance at 1400 MeV in the  $K^\pm K_s \pi^\mp$  system [1], which they named E-meson. It was discovered in  $\bar{p}p$  annihilation at rest into  $(K^\pm K_s \pi^\mp) \pi^+ \pi^-$ . The mass was  $1425 \pm 7$  MeV and the width  $80 \pm 10$  MeV. Its quantum numbers were determined to be  $J^{PC} (I^G) = 0^{-+} (0^-)$  where the isospin  $I=0$  was not well determined but favoured over  $I=1$  [1]. The E decay rates were:

$$\frac{\Gamma(E \rightarrow K^*(892)\bar{K} + \bar{K}^*K, K^* \rightarrow K\pi)}{\Gamma(E \rightarrow a_0\pi, a_0 \rightarrow K\bar{K})} \simeq 1 \quad (1.2)$$

In the seventies and eighties different experiments found either a  $0^{-+}$  or a  $1^{++}$  state in the 1400 MeV region (Table 1.3) A state was also observed in radiative  $J/\Psi$  decay which was named “ $\iota$ ”. This state is a prime candidate for the  $0^{-+}$  glueball since it is produced by a gluon rich process. In 1989 the ASTERIX experiment [7] again found a  $0^{-+}$  in  $\bar{p}p$  annihilation. The decay mode was  $E/\iota \rightarrow \bar{K}^0 K^\pm \pi^\mp$ . It was also found in  $J/\Psi$  decay by DM2 [8] and by the Mark III collaboration [9], who suggested three particles, a  $0^{-+}$  around 1420 MeV decaying into  $a_0\pi$ , a  $1^{++}$  around 1440 MeV decaying to  $K^*(892)\bar{K}$  and a  $0^{-+}$  around 1490 MeV decaying exclusively into  $K^*(892)\bar{K}$ . A recent measurement in  $\bar{p}p$  annihilation is the one of the Obelix Collaboration [11] at LEAR with results similar to those observed by Mark III [9].

The  $K\bar{K}\pi$  mass spectrum around 1400 MeV is therefore quite confused and a detailed review of the experimental situation is beyond the scope of this work. It is not clear whether  $\iota$  (observed in  $J/\Psi$  radiative decay) and E (observed in  $\bar{p}p$  annihilation) are the same state. Since this work shows that E is  $0^{-+}$  like

Table 1: The  $E/\iota$  observed in various experiments

Experiment	Reaction	$J^{PC}$	$E/\iota$ decay	Mass MeV	$\Gamma$ MeV	Ref
CCDF	$\bar{p}p \rightarrow K\bar{K}\pi\pi$	$0^{-+}$ $0^{-+}$	$a_0\pi \rightarrow K\bar{K}\pi$ $\bar{K}K^*(892)$	$1425 \pm 7$	$80 \pm 10$	[1]
Crystal Ball	$J/\Psi \rightarrow \gamma K_s^0 K^\pm \pi^\mp$	$0^{-+}$	$a_0\pi \rightarrow K\bar{K}\pi$	$1440_{-15}^{+10}$	$50_{-20}^{+30}$	[12]
MPS	$\pi^- p \rightarrow K\bar{K}\pi n$	$0^{-+}$	$a_0\pi \rightarrow K\bar{K}\pi$	$1421 \pm 2$	$60 \pm 10$	[13]
KEK	$\pi^- p \rightarrow \eta \pi^+ \pi^- n$	$0^{-+}$	$a_0\pi \rightarrow \eta \pi \pi$	$1420 \pm 5$	$31 \pm 7$	[14]
Mark III	$J/\Psi \rightarrow \omega K\bar{K}\pi$	$1^+$	$K\bar{K}\pi$	$1442_{-18}^{+15}$	$40_{-14}^{+18}$	[15]
ASTERIX	$\bar{p}p \rightarrow$ $\pi^+ \pi^- K^\pm \pi^\mp K^0$	$0^{-+}$	$a_0\pi \rightarrow K\bar{K}\pi$	$1413 \pm 8$	$62 \pm 16$	[7]
CELLO	$e^+ e^- \rightarrow$ $e^+ e^- K_s^0 \bar{K}\pi$	$1^{++}$	$\gamma\gamma \rightarrow K_s^0 K\pi$	$1425 \pm 10$	$42 \pm 22$	[16]
DM2	$J/\Psi \rightarrow \gamma K\bar{K}\pi$	$0^{-+}$ $0^{-+}$ $1^{++}$	$a_0\pi \rightarrow K\bar{K}\pi$ $\bar{K}K^*(892)$ $\bar{K}K^*(892)$	$1459 \pm 5$ $1421 \pm 14$ $1462 \pm 20$	$75 \pm 9$ $63 \pm 18$ $129 \pm 41$	[8]
WA 76	$(\pi^+/p)p \rightarrow$ $(\pi^+/p)K\bar{K}\pi p$	$1^{++}$	$\bar{K}K^*(892)$	$1430 \pm 4$	$58 \pm 10$	[17]
Mark III	$J/\Psi \rightarrow$ $\gamma K_s^0 K^\pm \pi^\mp$	$0^{-+}$ $1^{++}$ $0^{-+}$	$\bar{K}K^*(892)$ $\bar{K}K^*(892)$ $a_0\pi \rightarrow K\bar{K}\pi$	$1490_{-18}^{+14}$ $1443_{-6}^{+8}$ $1416_{-9}^{+11}$	$91_{-49}^{+69}$ $68_{-20}^{+30}$ $54_{-32}^{+39}$	[9]
	$J/\Psi \rightarrow \gamma \eta \pi^+ \pi^-$	$0^{-+}$	$a_0\pi \rightarrow \eta \pi \pi$	$1400 \pm 6$	$46 \pm 13$	[18]

the  $\iota$ , I shall use the generic name  $E/\iota$  for the structure observed at 1400 MeV throughout this work.

Table 1.3 shows a selected overview of the experimental situation. For more details I refer to the compilation of the Particle Data Group [10].

We are searching for the decay mode  $E/\iota \rightarrow \pi\pi\eta$  which was not observed so far in  $\bar{p}p$  at rest, to clarify the following questions:

- Can we confirm the  $0^{-+}$  state observed in  $\bar{p}p$  [1] [7] at 1420 MeV, but now decaying to  $\eta\pi\pi$ ?
- Is there a  $1^{++}$  contribution?
- What is the branching ratios for the decay mode  $E/\iota \rightarrow a_0\pi$  with  $a_0 \rightarrow \eta\pi$ ?
- What is the branching ratio for the predicted but not yet observed decay mode  $E/\iota \rightarrow \eta(\pi\pi)_{s\text{-wave}}$ ?

Figure 1.2: SU(3) nonet for the pseudoscalar mesons made of u, d, s quarks.  
 N=1: ground state N=2: first radial excitation.

Looking at the first excited state of the  $0^{-+}$  nonet shown in figure 1.2 (see also figure 1.1) one observes that the  $s\bar{s}$  state is missing. So another theoretical question has to be added: Is the  $E/\iota$  particle this missing  $q\bar{q}$  meson, or is it a glueball, in which case the 1490 MeV state [9] would be the missing  $\bar{q}q$  meson.

To answer some of these questions we collected a large data set on the  $4\pi\eta$  final state, containing two  $E/\iota$  samples with approximately 5000 reconstructed events for each  $\bar{p}p \rightarrow (\pi^+\pi^-)E/\iota(\rightarrow \pi^0\pi^0\eta)$  and  $\bar{p}p \rightarrow (\pi^0\pi^0)E/\iota(\rightarrow \pi^+\pi^-\eta)$ .

# Chapter 2

## Experiment

### 2.1 Apparatus

The Crystal Barrel experiment is located at the low energy antiproton ring (LEAR) at CERN. It was proposed in 1985 [19] and came into operation in 1989. Its main purpose is to measure  $\bar{p}p$  annihilation at rest, but it was foreseen from the beginning to take data with  $\bar{p}$  annihilating in flight (maximum LEAR momentum: 2 GeV/c). The final state particles in  $\bar{p}p$  annihilation are mainly  $\gamma$ ,  $\pi^{+-}$ ,  $K^{+-}$  and  $K_L$ . Electrons and muons are rare. In  $\bar{p}d$  (deuteron) annihilation one can observe recoil protons and neutrons, too.

We are interested to resolve the different meson states, and we would like to study rare channels. We therefore need high statistics, good energy and momentum resolution of the final state particles. Thus a detector should fulfil the following requirements:

- identification of charged and neutral particles.
- separation of (charged)  $\pi$  and K.
- good momentum resolution for charged particles.
- good energy and angular resolution for photons.
- low energy threshold for photon detection
- high detection efficiency over  $4\pi$  solid angle.
- an efficient trigger system with small dead time.
- the ability to process high beam intensities and a fast readout.

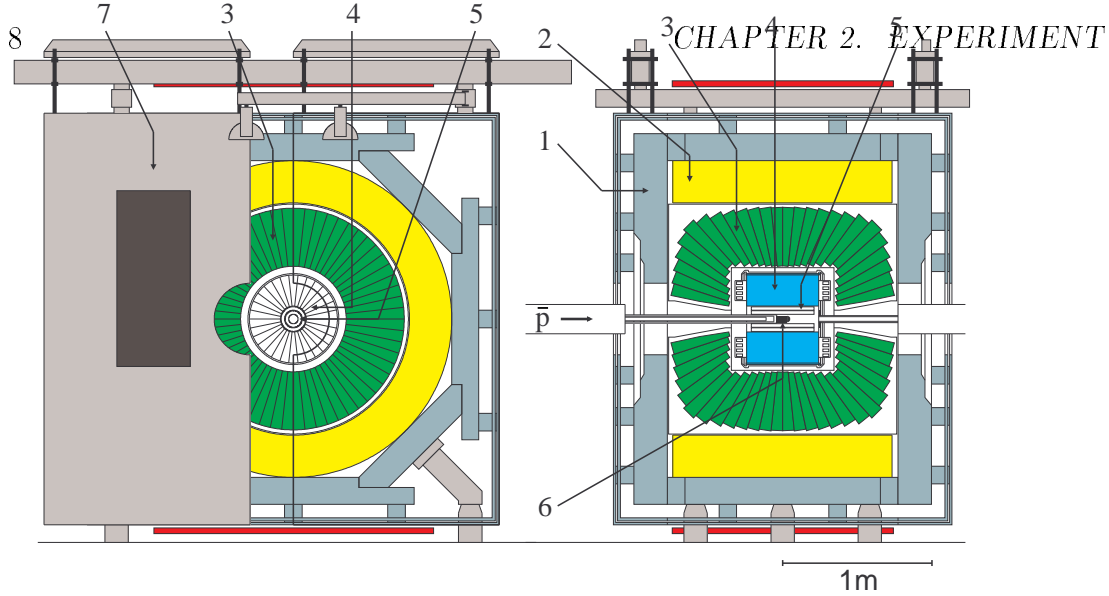


Figure 2.1: The Crystal Barrel experiment: overview

- 1: magnet yoke    2: magnet coils    3: calorimeter    4: jet drift chamber  
 5: proportional chamber    6: liquid hydrogen target    7: one half of the endplate

The Crystal Barrel detector fulfils most of these requirements. The layout of the experiment is shown in figure 2.1 and a detailed description can be found in [20]. Two multiwire proportional chambers (PWC) are located around the target, surrounded by a jet drift chamber (JDC) and the crystal calorimeter. A solenoid magnet (1.5 T) produces a homogeneous field over the detection volume. The two PWCs can be replaced by a silicon vertex detector, which will be installed in 1995. Its main purpose is to trigger on  $K_s$ -decays into  $\pi^+\pi^-$ .

### 2.1.1 Target

Most of the data, including the present data sets, were taken in liquid hydrogen with a  $\bar{p}$  beam momentum of 200 MeV/c. The  $\bar{p}$  stop after 2 cm in the center of the target, are captured by the protons to form antiprotonic atoms and then annihilate at rest with the protons. The target is shown in figure 2.2. It has a length of 4 cm and a diameter of 17 mm. Every incoming  $\bar{p}$  goes through a set of three beam counters. After crossing the small proportional wire chamber which has a very high efficiency ( $> 99\%$ ) the  $\bar{p}$  traverse a small silicon counter which restricts the beam size of the accepted  $\bar{p}$  to 0.5 cm. There is also a fourfold

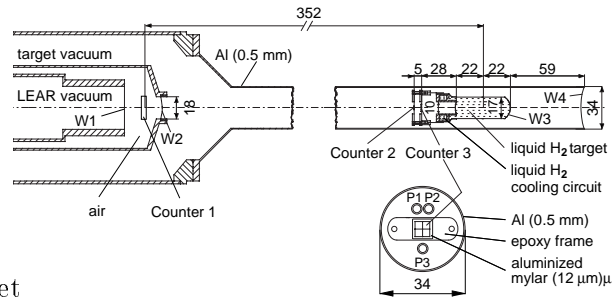


Figure 2.2: Liquid hydrogen target

Counter 1: Proportional Wire Chamber used to reject pile up events

Counter 2: Small silicon counter restricting the beam size to 0.5 cm.

Counter 3: Silicon counter segmented into 4 sectors to control if the beam axis is centered on the target.

The coincidence of counter 2 and 3 is used to start the trigger.

segmented silicon counter to measure online how well the beam is centered. Figure 2.3 shows the vertex distribution as it is reconstructed by the JDC for events which are accepted by the 2 prong trigger (see 2.2.1).

The left picture of figure 2.3 shows that the  $\bar{p}$  are stopped at an average distance of 1.7 mm upstream of the center of the detector. The width of 4.7 mm is determined mainly by the z-resolution of the JDC. We find that the beam is symmetric perpendicular to the beam axis, has the same width in x and y, and is centered almost exactly on the detector axis. The radial hit distribution  $r$  is shown in the right picture, with a fit to the function  $\text{Const} \cdot r \cdot \exp(-\frac{1}{2}r^2/\sigma^2)$ , with  $\sigma = 3.0$  mm. This is close to the size of the entrance counter 3.

The Crystal Barrel experiment also collected some data with liquid deuterium using the same target. A second target designed for gaseous hydrogen at a pressure of 10 bar was recently installed and used to accumulate data for annihilation from the atomic P-states.

### 2.1.2 Multiwire Proportional Chamber (PWC)

The proportional chambers were built in the mechanics workshop of our institute. The two chambers which are read out only from one side (no z-information) are mainly used for trigger purposes. They cover a solid angle of 98.6% for the inner

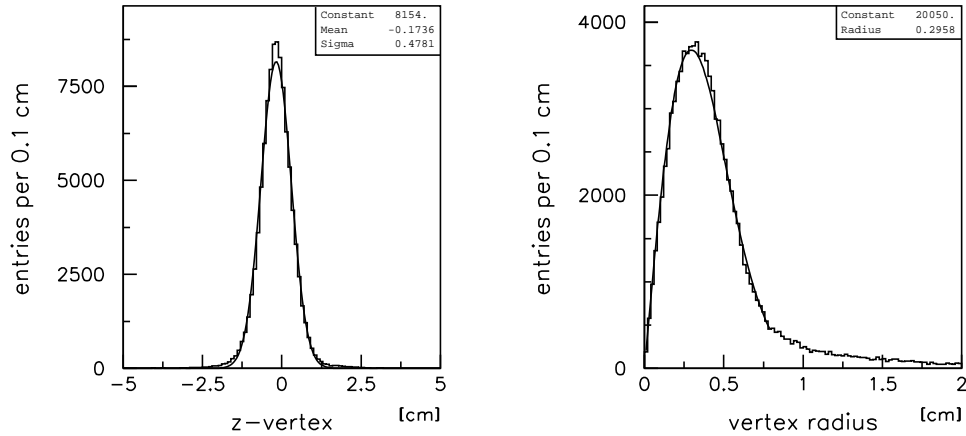


Figure 2.3: Distribution of the vertex reconstructed by the JDC

Left: along the beam axis ( $z$ ).  
 Right: perpendicular to the beam axis ( $r$ ).

and 96.4% for the outer chamber, respectively, and have 90 / 150 signal (anode) wires. The wires are lying parallel to the beam axis at a radius of 2.5/4.1 cm and have a wire spacing of 1.75/1.72 mm. The wires have a diameter of  $15\mu\text{m}$  and are strung with a tension of 30 g. The distance between anode and cathode is 3.5 mm. We use a gas mixture of 69.5% argon, 30% ethane and 0.5% freon. We find an efficiency of more than 99% [21]. A detailed drawing is shown in figure 2.4.

A first set of chambers built with 120 / 180 wires, had only a short lifetime, because of a strong ageing effect and an extreme design radius of 2.5/4.1 cm, 1.1/1.3 mm wire pitch and the necessity of large pulses, because we need 3 m of (shielded coax) cable between preamplifier and chamber. The main problem was that their aluminum cathode of  $0.5\mu\text{m}$  thickness (vapor deposited on a  $25\mu\text{m}$  capton foil) was too thin. After some weeks of running time we found (burned) holes in the aluminum which covered 10% of the surface. We solved this problem by rebuilding the chambers with a reduced number of wires, and a cathode foil with a thickness of  $20\mu\text{m}$ . At the same time we changed the design of the readout prints. In order to improve the fixation of the signal wires we soldered them twice at each end. The chambers were tested again [22] and we obtained best results with the same gas mixture as before. We had initially many electrical sparks, and several of the wires broke. But after one year the chambers became stable and they have been running since two years without any problems. The PWC readout is provided by the LeCroy PCOS III system.

Figure 2.4: Drawing of the upstream end of the two PWC's.

A: HV-plug	B: ground-plug	C: outer shield	D: cathode foil
E: signal wire	F: print	G: signal cable	H: O ring
I: hole for HV pin			

### 2.1.3 Jet Drift Chamber (JDC)

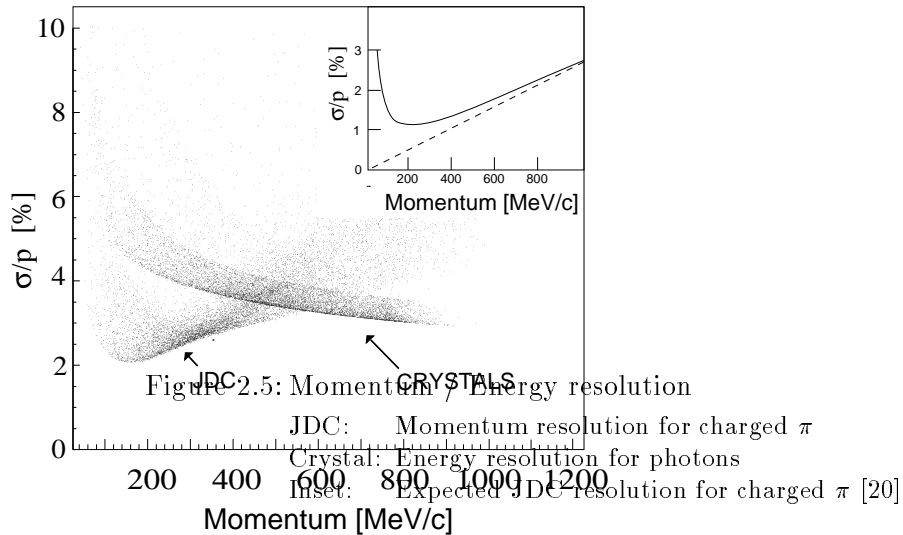
Flight direction and momentum of charged particles in the final state are determined in the JDC which measures their positions along the track. The chamber covers a solid angle of 94% for the innermost and 64% for the outermost of the 23 layers. It is cylindrical with a length of 40 cm and a diameter of 51 cm, and is divided in 30 azimuthal sectors. We use a drift field of 1.1 kV/cm, a magnetic field of 1.5 T and a gas mixture of 90% carbon dioxide and 10% isobutane at atmospheric pressure. This leads to a drift velocity of 9.5 mm/ $\mu$ s and a Lorentz angle of 7°. The right/left ambiguity in the track reconstruction is resolved by an azimuthal staggering of the sense wires of  $\pm 200\mu\text{m}$ . The resolution ( $\sigma$ ) in the  $r$ - $\phi$  plane is 120  $\mu\text{m}$ . Using the charge division of signals at the end of the wires, we measure the  $z$ -coordinate with a resolution of  $\sigma=7$  mm.

Figure 2.5 shows the momentum resolution of the JDC for charged pions, compared to the photon energy resolution of the calorimeter. These resolutions were obtained by comparing the measured momenta to the fitted momenta in kinematically overconstrained channels like  $\bar{p}p \rightarrow 2\pi^+2\pi^-$  and  $\bar{p}p \rightarrow \pi^0\pi^0 \rightarrow 4\gamma$ . The resolution of the JDC is close to its design value (inset) and is comparable to or even better than the crystal resolution for photons at low momenta.

### 2.1.4 Crystal Calorimeter

The electromagnetic calorimeter provides an efficient photon detection with a good energy and spatial resolution over an energy range from 10 to 2000 MeV. This is important, because about 90% of the events have a final state which contains at least one photon. The calorimeter consists of 1380 CsI(Tl) crystals arranged in 26 rings and covers a solid angle of 97%. Due to shower energy leaking from the crystals close to the holes of the beam pipe, photons can only be properly measured if they shower in rings 2 to 25 (solid angle 95%). Each crystal has a length of 300 mm, which corresponds to 16 radiation lengths, and covers a polar and azimuthal angle of 6°. The azimuthal angle for the three rows closest to the beam axis is 12°.

The readout is made by photodiodes, because the calorimeter lies inside the magnet. A wavelength shifter is connected to the rear end of each crystal. It absorbs the light, which peaks for CsI(Tl) at a wavelength of 550 nm, and re-emits it in a small band between 600 and 650 nm, where the absorption of the photodiode is higher. In addition it works like a light guide, collecting and transporting the light to the photodiode. The photodiode therefore can have a much smaller size which leads to a reduced electronic noise.



The crystal information is read out by two ADC systems in parallel. The Le Croy 2282 system with 4096 channels over a limited range (0-400 MeV) has a high sensitivity (0.1 MeV/channel). The Le Croy 4300-B Fera system with 2048 channels over the full range (0-2000 GeV, 1 MeV/channel) provides a fast readout for the trigger system (section 2.2.1 and 2.2.2).

## 2.2 Trigger

The Crystal Barrel experiment has a complex trigger system which is presented in figure 2.6 and described in more details in [20]. To collect the present data we used, for the first time, all levels of the trigger system (including the hardwired FACE processor and the software trigger).

### 2.2.1 Hardware Trigger

For the minimum bias trigger we request that a  $\bar{p}$  stops in the target. In order to start the trigger process we use the information of the small silicon counter (counter 2 in figure 2.2) in coincidence with the signal which results by an 'OR'

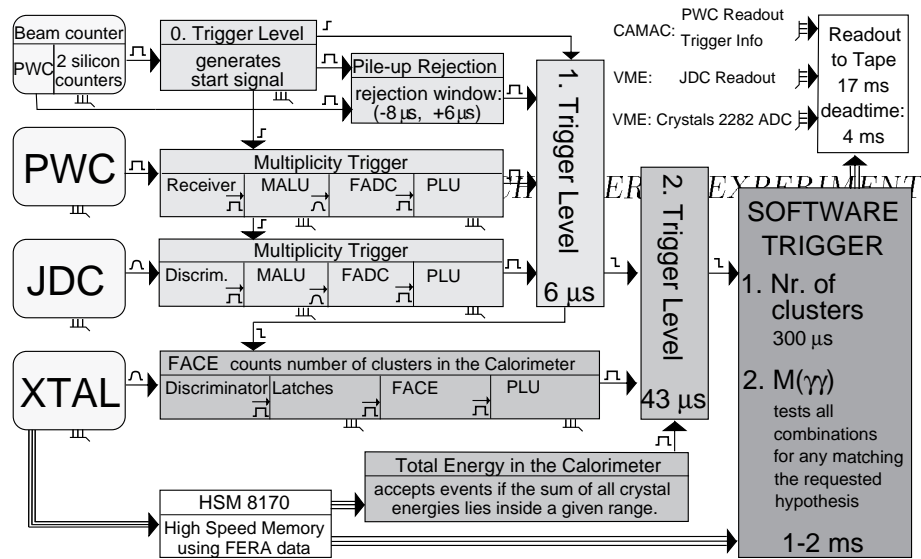


Figure 2.6: The Crystal Barrel Trigger Logic

PWC: 2 Proportional Wire Chambers, 90 resp. 150 anode wires

JDC: Jet Drift Chamber, 30 sectors each with 23 wires per layer

XTAL: CsI(Tl) Crystals, 1380 channels

MALU: (Multiplicity Arithmetic Logic Unit) can be used in 2 modes:

1. counts number of hits at the entrance.
2. connects neighbored hits to a cluster and counts number of clusters.

The output signals of the different units are proportional to the multiplicity and are summed to give the total signal.

FADC: Flash Analog to Digital Converter.

PLU: Programmable Logical Unit.

FACE: Fast Cluster Encoding

of the 4 signals of the fourfold counter (counter 3). This helps to suppress noise and enables us to use thin counters which have a low signal amplitude.

Trigger level 1 contains the multiplicity triggers of PWC and JDC and the pile-up rejection. The most efficient device to select the number of charged particles ( $n$ -prong trigger) is the multiplicity trigger system which uses the two multiwire proportional chambers, because of their large solid angles (99% and 96%) and their high efficiencies. As part of my diploma work I had built and tested this trigger [21]. For the data collected for the present thesis we actually used the

multiplicity trigger system of the jet drift chamber (JDC), due to a hardware failure in the PWC readout electronics. The trigger information is extracted from layers 2-5 (the innermost layer 1 has a somewhat reduced efficiency) and we accept events with 2 hits in each of the 4 layers. To increase the reconstruction efficiency and improve the momentum resolution we ask for long tracks accepting events with 2 hits in layers 20 and 21.

If one runs with a high beam rate to saturate the readout, as for the present data set (see section 2.2.2), it is possible to reject pile-up events on the trigger level. If the proportional chamber in the beam line detects a second  $\bar{p}$  inside a time window of  $-8 \dots +6 \mu s$  the event is rejected. The decision time of this first trigger level is  $6 \mu s$ .

Trigger level 2 contains the FACE and a hardware total energy sum. The FACE (FASt Cluster Encoding) processor counts the number of clusters registered in the calorimeter. The crystal receivers have for each channel a separate output, from where the unshaped signal (steep rising edge) is sent to a discriminator. With the threshold which can be set for all channels simultaneously one can choose the minimum energy deposit per crystal used in the FACE. The signals are latched in special modules. The latch modules can also be read out via CAMAC. Thus we could compare them to the signals seen by the (FERA) ADC and control the hardware during the run. In the FACE processor itself the crystals are mapped onto a matrix of 26 rows and 60 columns. For all crystals with energy deposits above threshold (20 MeV) the corresponding bit in the matrix is set. A hardwired algorithm now finds clusters of neighbouring bits [20].

The pedestal subtracted energy information of each crystal (FERA data) is sent to a HSM 8170 high speed memory. This is read from a hardware adder which calculates the sum of all ADC entries, which is proportional to the total energy measured in the calorimeter.

Trigger level 2 was started when trigger level 1 accepted the event. The decision time of level 2 is  $43 \mu s$ . This time could be reduced by  $6 \mu s$ , however, starting levels 1 and 2 simultaneously and resetting the FACE, if required.

### 2.2.2 Software Trigger

The software trigger installed on a FORCE computer with a 68040 (25 MHz) processor receives the energy information of the crystals again from the HSM 8170 memory. The minimal energy per channel as well as the energy resolution is 1 MeV (FERA data). For a typical event it needs  $200 \mu s$  to read and decode the data into a useful format. Energies of neighbouring crystals are added to form the cluster energy with the following algorithm: To a crystal with more

energy than a specified minimum  $N_{min}$  the energy of all 8 neighbours are added. If one of them again has more energy than  $N_{min}$ , his neighbours are added too. (Each crystal information is used only once of course). The center of the cluster is determined by the crystal with the highest energy. This means the trigger can separate two clusters if there is 1 crystal below  $N_{min}$  inbetween. Clusters with less than a specified minimal energy  $E_{min}$  are neglected. For the present data the software trigger needs approximately 300  $\mu s$  to calculate the number of clusters.

In a next step the invariant mass of all possible  $\gamma$ -pair combinations is calculated. One has to define mass windows for the  $\pi^0$  and  $\eta$  masses, and the maximum number of allowed  $\pi^0$ ,  $\eta$  and 'none' (invariant mass combinations which do not fit into any of these windows). The event is rejected if the trigger does not find any combination with the specified number of mesons. The decision time lies between 1 and 2 ms.

The software trigger was written with the aim of triggering on final states which contain resonances decaying to  $\eta$  mesons and was used for the first time in the present work. It was necessary to debug it and to test the performance. The speed is surprisingly high, due to the fact that both cluster and meson finding algorithms are programmed recursively. Thus an extremely short program code (written in C) was achieved which fully fits into the CPU-cache.

### 2.2.3 Trigger on the $\pi^+\pi^-\pi^0\pi^0\eta$ Final State

In order to find the trigger parameters (mass windows, thresholds, etc) which enable us to collect the maximum number of reconstructable  $\pi^+\pi^-\pi^0\pi^0\eta$  events on tape in the allocated beam time, we used events from the minimum bias data set (e.g.  $\bar{p}$  stop only), for which the offline reconstruction found that they had the  $\pi^+\pi^-\pi^0\pi^0\eta$  topology. The goal was to optimize both the enrichment factor

$$\text{enrichment} = \frac{\text{fraction of reconstructable events of triggered data}}{\text{fraction of reconstructable events of min. bias data}} \quad (2.1)$$

and the data acquisition speed. I determined the enrichment factor of each trigger level by running the  $\pi^+\pi^-\pi^0\pi^0\eta$  events through the trigger simulator which is described in detail in section 3.4.

The data acquisition speed for minimum bias events has been increased from 10 Hz at the beginning of the experiment (1990) to the present 40 Hz. A major progress was to buffer the events before writing them to tape. Using the fraction

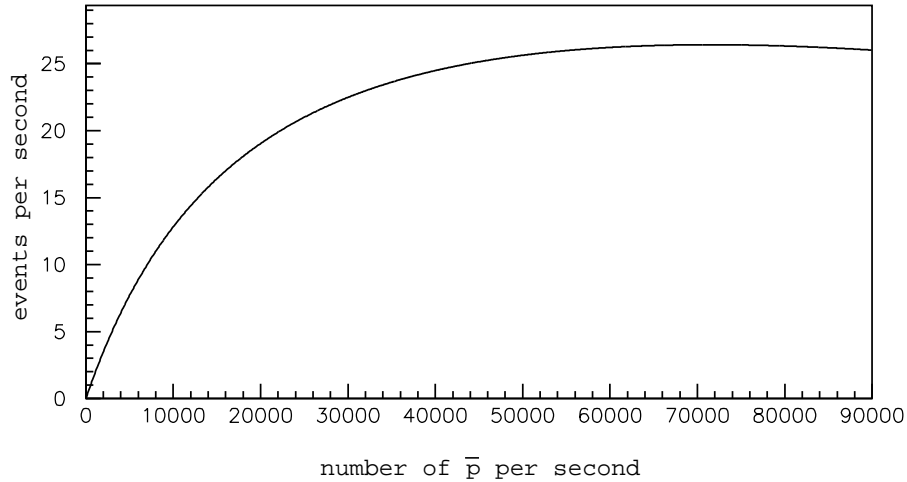


Figure 2.7: Calculated data acquisition speed  $S$  to tape for the trigger parameters given in Table 2.1

of lifetime to total time  $L$ , one can calculate the data acquisition speed  $S$ :

$$L = \text{Min} \left\{ \frac{1}{1 + n_0 * \sum_{i=1}^5 \prod_{j=1}^i f_j * t_{i+1}}, \frac{1}{1 + n_0 * \prod_{j=1}^5 f_j * t_R} \right\}$$

$$S = L * n_0 * \prod_{j=1}^5 f_j \quad (2.2)$$

The variables are  $f_j$  the fraction of the data which is tested and accepted by trigger level  $j$ ,  $t_i$  the decision time of trigger level  $i$  and  $n_0$  the number of incoming  $\bar{p}$  per second. The numbers were taken from table 2.1:  $i=2$ : JDC/pile-up  $i=3$ : FACE/energy-sum  $i=4$ : software cluster  $i=5$ : software meson. Some additional parameters are used, namely  $f_1 = e^{-n_0 * p}$   $p$  is the pile-up window with a length of  $14 \mu s$ ,  $t_6$  is the time which the readout needs to write the data into the buffer and  $t_R$  is the time which is needed to write the data on tape. For data taking we restricted the rate to a maximum of 30000 incoming  $\bar{p}$  per second.  $S$  is plotted in figure 2.7 for the trigger parameters shown in table 2.1 and is in nice agreement with reality.

We collected some small data samples using the 2-prong trigger and enabled the FACE with different threshold levels. The data reconstruction accepted the

Table 2.1: Trigger requirements for the  $\pi^+\pi^-\pi^0\pi^0\eta$  final state

The decision time includes the time for the fast reset. The data reduction is the fraction of the data which is tested and accepted by one level.  $N_{min}$ : Crystals below this energy separate 2 clusters. Clusters with energies below  $E_{min}$  are ignored.

Trigger Level	Specification	Window	Unit	Decision time	Data-reduct.	
hard-ware	1. level	pile-up rejection	-8 ... +6	$\mu s$	rate dependent	
		JDC layer 2-5	2 ... 2	prong	6 $\mu s$	0.075
		JDC layer 20,21	2 ... 2	prong		
	2. level	FACE threshold	18	MeV	43 $\mu s$	0.10
		FACE multiplicity	8	clusters		
	total energy	950-1700	MeV			
soft-ware	cluster-finding	number	8	clusters	0.3 ms	0.25
		$N_{min}$	13	MeV		
		$E_{min}$	18	MeV		
	meson-finding	$\pi^0$ window	121-149	MeV	1-2 ms	0.49
		$\eta$ window	520-578	MeV		
		max number of $\pi^0$	2			
		max number of $\eta$	2			
	max number 'none'	1				

largest fraction of events in the sample with a threshold corresponding to a minimum energy of 18 MeV per crystal. To determine the number of clusters which should be accepted from the FACE we collected data sets with a window of 8, 7-8, 7-9, 8-9 clusters in the FACE and found that 8 was the best choice. (The rate in case of 7-9 clusters was higher but the enrichment was substantially lower.)

The parameters for the total energy sum and the software trigger were then determined by the online trigger simulator. I loaded FERA data of good  $\pi^+\pi^-\pi^0\pi^0\eta$  events from an early minimum bias data sample into the HSM memory (figure 2.6) and ran them through the hardware total energy sum and the software trigger. This made it possible to determine the trigger parameters which are given in table 2.1) without wasting  $\bar{p}$ .

The reason for getting the best results by asking for 8 clusters on a final state with 6  $\gamma$  is simply because we cannot distinguish between the energy depositions of charged and neutral particles. The two charged particles are also the reason for allowing a "none" (see table 2.1). The invariant mass of their deposited energy in the calorimeter will rarely fall within the meson windows. In order to measure

in parallel the final state  $\pi^+\pi^-\pi^0\eta\eta$ , which has a very low branching ratio, we allowed a maximum of 2  $\eta$  in the software trigger (see section 4.5).



# Chapter 3

## Analysis Method

The data sets used in this work are listed in Table 3.1

### 3.1 Calibration

In a first step the z-coordinate of the JDC is calibrated using a 4-prong data set without magnetic field (DAT-V in table 3.1). For each of the 690 sense wires the amplitudes  $A_l$ ,  $A_r$  measured at both ends of the wires are combined in order to determine the z-coordinate by using the charge division method:

$$z = z_0 + z_L * \frac{A_l - \alpha * A_r}{A_l + \alpha * A_r} \quad (3.1)$$

where  $z_0$  is the location of the center and  $z_L$  the electrical length of the wire and  $\alpha$  is the relative gain between the two electronic chains.

The projections of the helicoidal tracks in a plane containing the detector axis (r-z plane) are in good approximation straight lines. For each wire the parameters  $z_0$ ,  $z_L$ , and  $\alpha$  are therefore determined by fitting straight lines to good, preselected tracks.

The radial coordinates (drift times) are calibrated using the data set DAT-VI from the two-body final states  $\pi^+\pi^-$  and  $K^+K^-$ . These particles are produced monoenergetically with a momentum of 927.8 MeV/c for pions and 797.9 MeV/c for kaons. This allows to fit the two tracks with one single helix and provides a strong constraint. With the electrostatic simulation program Garfield [23] drift time tables are generated for different drift velocities (which depend on the the current atmospheric pressure and the gas temperature) for each cell type. The fit tries to find the best set of tables by minimizing the width of the peaks in the measured momentum distribution of the monoenergetic kaons and pions for run

Table 3.1: Data sets collected during the run in October 1993.  
 DAT V-VII were used for apparatus calibration.

	description of the dataset	nr. events
DAT-I	trigger on $\pi^+\pi^-\pi^0\pi^0\eta$ final state (all trigger levels)	5'832'973
DAT-II	minimum bias	122'971
DAT-III	2 prong and pile up rejection (1. trigger level)	136'800
DAT-IV	FACE and total energy sum (2. trigger level)	150'000
DAT-V	4 prong (1. trigger level) without magnetic field	$\sim 50'000$
DAT-VI	2 collinear $\pi$ ( $\bar{p}p \rightarrow \pi^+\pi^-$ ) 2 prong and software trigger	5000
DAT-VII	0 prong (1. trigger level)	$1.2 \cdot 10^6$

periods with equal atmospheric pressures. The momentum resolution  $\sigma_p/p$  for a single trajectory of two collinear tracks in the  $\pi^+\pi^-$  final state (data set DAT-VI) achieved by this method is 2% at  $p=928$  MeV/c. The momentum resolution for the four-prong final state  $\pi^+\pi^-\pi^+\pi^-$  is shown in figure 2.5 where the kinematic fitted momenta are compared to the measured momenta.

The calibration of the electromagnetic calorimeter is done with the all neutral data set DAT-VII. Looking at the  $\gamma\gamma$  invariant mass distributions one observes a strong  $\pi^0$  peak. Taking all photons which entered a given crystal one can calibrate the energy scale by using the  $\pi^0$  mass as a constraint. The energy resolution  $\sigma_E/E$  achieved by this method is  $2.5\%/(E[\text{GeV}])^{1/4}$  (figure 2.5).

## 3.2 Event Reconstruction

The Crystal Barrel detector was designed to measure the energy and momentum of all final state particles (except  $K_L$  and neutrons in  $\bar{p}d$  annihilation). The event reconstruction program calculates the particle momenta and energies and stores them in form of a ZEBRA data bank [24].

We use 100 MHz FADC to sample the JDC pulses. This information is converted to positions in space using the drift times relative to the start time. The pattern recognition algorithm tries to find track segments, first in the r-z plane, then in the r- $\phi$  plane. A forward/backward projection algorithm is applied to pick up additional hits. The parameters of a circle fit which matches broken segments of a track, are passed to a helix fitting algorithm which performs a full three dimensional helix fit for each track and determines momentum, charge and distance of closest approach for each pair of tracks. A vertex fit is applied for events with more than one track, forcing the origin of all tracks to a common

point. The vertex distribution is shown for the 2-prong data set (DAT-III) in figure 2.3.

The signals of the 2282 and the FERA ADCs are converted into energies for each crystal, rejecting depositions below 1 MeV. A search is made for clusters of neighbouring crystals, which need to have a total energy of at least 20 MeV to be accepted. Local energy maxima within a cluster (e.g. having more than 20 MeV deposit in their central crystals) generate separate photons. These local maxima can be caused (i) from overlapping  $\gamma$  showers or (ii) from fluctuations within the shower. The  $\gamma$  direction is obtained by calculating the center of gravity of the shower e.g. by weighing the crystal positions by the energy deposit. Clusters originated from charged particles are removed, if the extrapolated trajectories of the tracks can be associated with a cluster in space. In the present data set DAT I-II 90% of the tracks can be matched to a cluster in the calorimeter.

There are three ways that, after the reconstruction, energy deposits which do not originate from a photon are still left in the calorimeter.

1. A pion traveling through the barrel sometimes kicks out a neutron, which can produce an energy deposit at a different location (the so-called split-off). In the case of collinear events (DAT-VI) one finds 0.5 split-offs per pion!
2. The reconstruction could not match the trajectory of the pion with its energy deposit.
3. Satellite clusters from shower fluctuations can have more than 20 MeV. In case of the all neutral six photon final state one finds such a shower fluctuation for 5% of the photons.

In the first and the second cases total energy and total momentum of the event are modified. A kinematic fit routine with constraints on total momentum and energy (4C fit) will find a higher confidence level if it uses only the real photons. We therefore run every event through an algorithm (CBDROP) which removes 0, 1, and all possible combinations of 2 photons, submits the remaining particles to the kinematic fit and returns the photons of the most probable combination. We found for the data set DAT-I, for events where CBDROP found 6 photons that 58% of the events had originally 6, 29% 7 and 13% 8 photons in the calorimeter.

The shower fluctuations should be merged with the main cluster. Monte Carlo studies have been done for different final states to find algorithms suitable to identify them, but we found that the input parameters which separate shower fluctuations and real photons must be tuned separately for each final state. For the high multiplicity channels like  $\pi^+\pi^-\pi^0\pi^0\eta \rightarrow \pi^+\pi^-6\gamma$ , the photon energies

are relatively low and therefore shower fluctuations (their energies scale roughly with the photon energies) are less important than for low multiplicity channels. Corrections for shower fluctuations have therefore been ignored in this analysis.

### 3.3 Monte Carlo Simulation

Real data are compared to Monte Carlo data obtained by first assuming phase space distribution of the final state  $\pi^+\pi^-\pi^0\pi^0\eta$ . The Monte Carlo program takes into account detector and reconstruction inefficiencies. The Monte Carlo simulation of the detector is based on the CERN software package GEANT version 3.15 [25]. All components of the detector are modelled, and the interactions of annihilation particles are taken into account. GEISHA [26] is used to simulate the hadronic interactions and GEANT the electromagnetic showering of the particles in the various detector components. After producing signals for each subdetector the simulated events are stored in the same data format as the real events. The generated Monte Carlo data sets are listed in table 4.2 (section 4.4).

### 3.4 Performance of the Trigger

In order to properly simulate the trigger I first determined the efficiency and the noise for all detector and trigger components. I ran the Monte Carlo events through the simulation described below to guarantee that they are treated in the same way as the real data events. We used the calibration data sets given in table 3.1 to determine the enrichment factors (defined in 2.1) of the different trigger levels. The enrichment factors are given in table 3.2.

#### 3.4.1 1. Trigger Level (Hardware)

Figure 3.1 shows the efficiency and the noise of the chamber and the trigger electronics. We used events from the minimum bias data set (DAT-II) with two long tracks to calculate the efficiency of the chamber. The efficiency of each JDC wire was determined by looking at the two adjacent wires in the same sector (above and below the corresponding layer). I calculated the fraction of events with two neighbouring hits for which the middle wire had fired, which is the efficiency shown in figure 3.1a. The first and the last layers have of course no entries.

To calculate the noise of the chamber, the hits of each wire  $j$  for all events of the minimum bias data set were summed ( $M_j$ ). After correcting  $M_j$  for the

solid angle of the different layers, the noise  $N_j$  was calculated according to 3.2 and plotted in figure 3.1b.

$$N_j = \Theta \left( \left[ M_j - \frac{\sum_{i=1}^{690} M_i}{690} \right] - 0.05 \right) \quad (3.2)$$

$\Theta(x)$  is the step function which is 0 for  $x < 0$  and 1 for  $x > 0$  and takes noise into account if it is larger than 5%.

In order to calculate the efficiency and the noise of the JDC multiplicity trigger we used the trigger information from the MALU board (figure 2.6) which was read out. I used again events from the minimum bias data set where the reconstruction program found two long tracks. Efficiency and noise were calculated according to 3.3 and plotted in figure 3.1c and 3.1d.

$$\begin{aligned} \text{efficiency}^j &= \frac{\sum_{i=1}^N \text{trigger}_i^j * \text{readout}_i^j}{\sum_{i=1}^N \text{readout}_i^j} \\ \text{noise}^j &= \frac{\sum_{i=1}^N (1 - \text{trigger}_i^j) * \text{readout}_i^j}{N} \end{aligned} \quad (3.3)$$

where  $\text{trigger}^j$  is 1 if the multiplicity trigger found a hit in wire  $j$  and  $\text{readout}^j$  is 1 if the readout found a hit in wire  $j$  otherwise they are 0.  $N$  is the number of events. If a Monte Carlo event is run through the trigger simulation, a random number generator takes the inefficiencies for each wire into account and also adds additional noise hits.

Table 3.2: Results of the trigger simulation for the  $\pi^+\pi^-\pi^0\pi^0\eta$  final state

The column “noise” gives the average probability of a noise hit for any of the wires/crystals. The JDC trigger efficiencies and noise concern only layers 2-5, 20 and 21.

Trigger level	Specification	Efficiency average per wire	Noise	Enrichment	MC-data reduction
JDC	chamber	96%	<0.05	6.3±0.9	0.18
	trigger	97%	0.001		
FACE Tot energy	discriminator & latch	98%	0.01	4.2	0.64
				1.05	0.99
Software	cluster finding	100%		3.5±0.4	0.73
Software	meson finding	99%			0.60
Overall				97±18	0.050

I also had to consider coherent noise ie. events which had always the same noise pattern. It was necessary to split the noise information of the trigger into 7 parts: 1-6 and more than 6 noise hits in the same event. All wire combinations which represent noise of more than 0.01 were stored.

The average chamber efficiencies and noise, as well as the trigger efficiencies and noise are indicated in table 3.2. Although the efficiencies of 96% for the chamber and of 97% for the JDC trigger are rather high, they nevertheless led to the big loss of good events in the trigger, due to the multiplicity 2 requirement on 6 JDC layers. This led to an efficiency of the JDC multiplicity trigger of  $0.96^{12} * 0.97^{12} = 42\%$ <sup>1</sup> Because I could not generate enough Monte Carlo events I used a constant chamber and trigger efficiency of 100% in the trigger simulation. The Monte Carlo efficiency then increases from 5% to 12%. To prove that local inefficiencies (figure 3.1a,c) do not introduce holes in the phase space distributions, I generated two data samples, one with the full trigger simulation (all trigger levels) according to figure 3.1a,c and one where the trigger efficiencies are set to a 100%. The  $\pi^+\pi^-\eta$  and  $\pi^0\pi^0\eta$  invariant mass projections are plotted in figure 3.2, normalized to the number of events of the smaller data set and show that the JDC inefficiencies do not cause distortions in the phase space distribution.

As pointed out earlier the PWC was not used due to a hardware failure in the readout electronics. Both chambers had however an efficiency of more than 99%. A multiplicity trigger using PWC, accepting exactly 2 clusters, and requesting 2 hits in layer 20 and 21 of the JDC would accept 1.7 times more good (reconstructable) events than the JDC trigger alone, i.e. the rate would go up (according to 2.2) by approximately 20%.

### 3.4.2 2. Trigger Level (Hardware)

The FERA data from the 2-prong data set (DAT-III in table 3.1) were used to determine the threshold value of each latch discriminator. Let me define as 'lost hits' those events with an energy  $> T$  for which the latch had not fired and as 'additional hits' the events with an energy  $< T$  for which the latch had fired. For each channel I calculated the sum S of the number of 'lost hits' and 'additional hits' events. I varied the threshold T (a low threshold produces many additional hits, a high threshold many lost hits) in order to find the smallest value for the sum S, which gave the optimum value for T. Using this threshold I then calculated separately for each channel the efficiencies of the discriminators (and the latches) which is the number of hits with a crystal energy above threshold T for which the

---

<sup>1</sup>The Monte Carlo data reduction of 0.18 in Table 3.2 of course includes the solid angle acceptance.

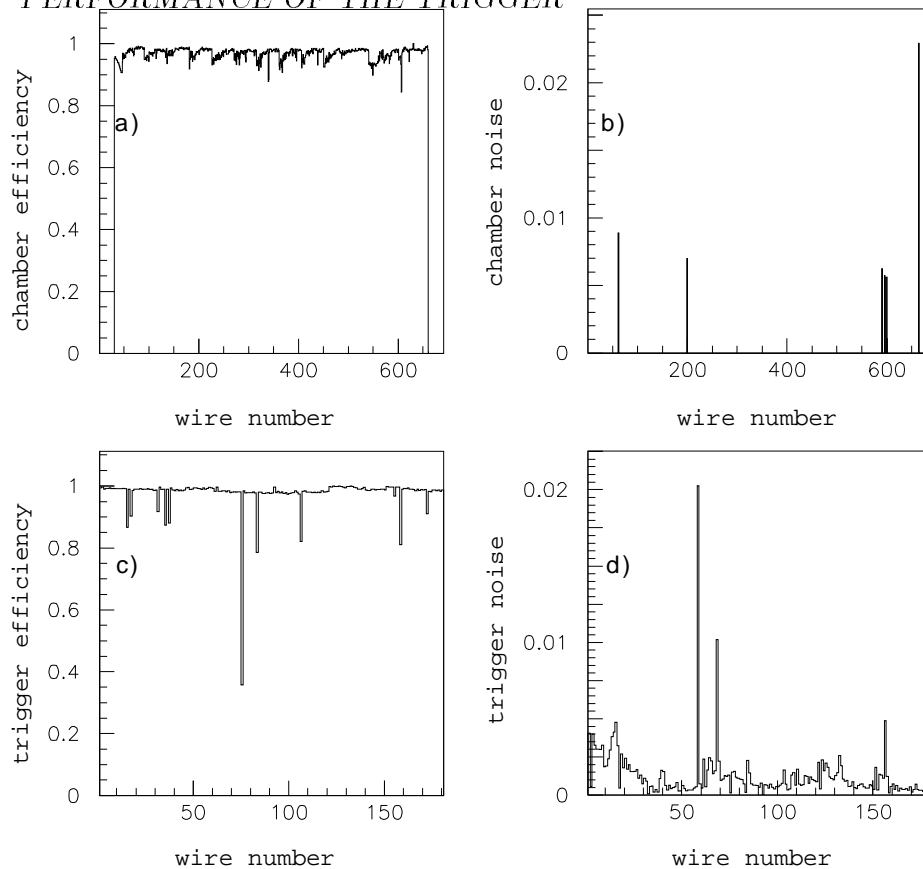


Figure 3.1: JDC chamber/trigger efficiency and noise

a), b) wire numbering scheme: layer 1: wires 1-30 ... layer 23: wires 661-690  
 c), d) wire numbering scheme: layer 2: wires 1-30 ... layer 5: wires 91-120  
 layer 20: wires 121-150, layer 21: wires 151-180

latch had fired, divided by the total number of all hits with crystal energy above threshold, and the noise which is the number of 'additional hits' divided by the total number of events. For real 2-prong events the latch information (which is read out for every event) was run through the simulation of the FACE algorithm. The result was compared with the actual multiplicity found by the FACE. At the time when we took the data, the FACE found the correct answer for 94% of the events, for the rest it found mostly one cluster less than the simulation did. The correlation is shown in figure 3.3 for a minimum bias run. It was impossible to trace the origin of this small discrepancy in the FACE hardware and therefore necessary to simulate the result.

The energies (FERA ADC simulation) of the Monte Carlo events for all crystals are used to simulate the discriminators and latches. After applying the

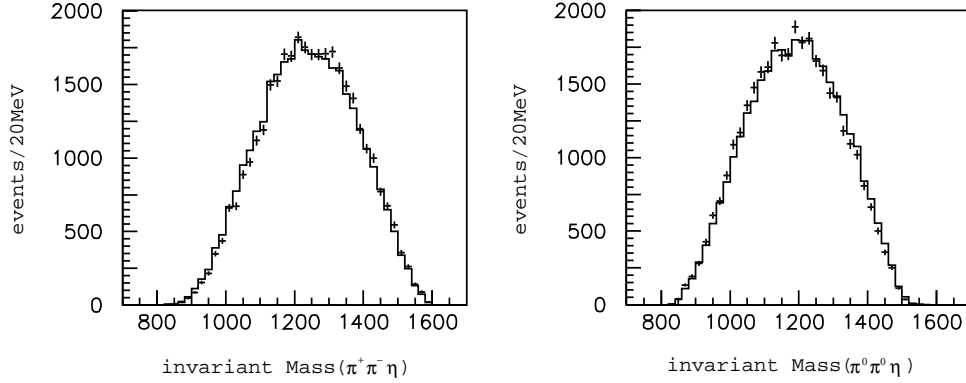


Figure 3.2: The  $\pi^+\pi^-\eta$  and  $\pi^0\pi^0\eta$  mass distributions for phase space distributed Monte Carlo events.

full line: JDC trigger simulation with 100% flat efficiencies.  
crosses: Simulation according to efficiencies shown in figure 3.1

threshold cut, a random number generator takes the inefficiencies into account for every channel and also adds additional noise hits. This information was ran through the simulated FACE algorithm. For all multiplicities (1-10) found by the simulation the probability for the small deficiency of the FACE was calculated and introduced in the Monte Carlo simulation.

The energy window used for the total energy sum simulation was determined by plotting the total energy registered in the calorimeter with the FERA ADC for the 2-prong data.

### 3.4.3 Software Trigger

The software trigger is written in C, and the original code used in the experiment was used in the trigger simulation. For the software trigger we used a preliminary calibration of the FERA ADCs, which I also installed in the trigger simulation. To test the simulation of the software trigger, I used the data set DAT-IV of table 3.1. The results of the software trigger and its simulation agree with the cluster finding algorithm and the agreement is better than 99% for the meson finding algorithm.

The FERA data produced from the Monte Carlo simulation were used with

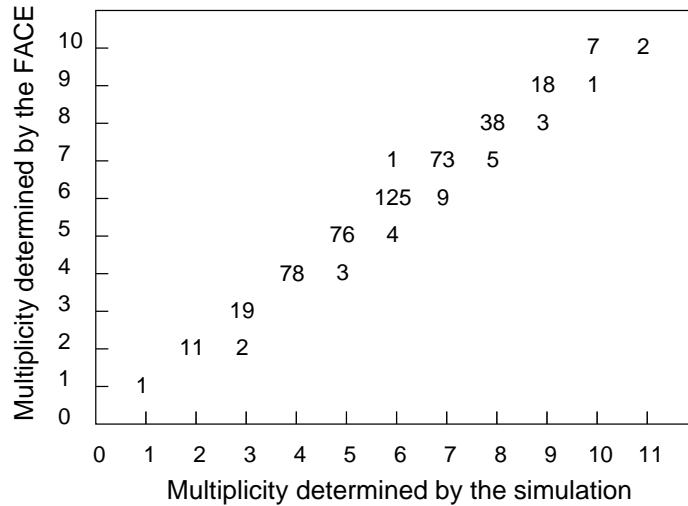


Figure 3.3: Performance of the FACE for a minimum bias run.

a special calibration. In order to simulate the reality as closely as possible I used also for Monte Carlo events the 'online' calibration which contains information about every crystal (pedestal and gain). It was therefore necessary to calibrate the simulated FERA amplitudes until the  $\pi^0$  mass distribution of the simulation and the real data peaked at the same value.

The reduction of the Monte Carlo events for the  $\pi^+\pi^-\pi^0\pi^0\eta$  final state, which resulted when they were passed through the simulation is given in table 3.2 for each trigger level. A total of 673'300 of the 5.8 Mio simulated events (12%) survived the trigger simulation with 100% JDC efficiency (see table 4.1 in the next section). For the background  $\pi^+\pi^-\pi^0\pi^0\pi^0$  final state, 15500 (3.6%) of the 430'000 events were accepted by the trigger as  $\pi^+\pi^-\pi^0\pi^0\eta$  events.



# Chapter 4

## The $\pi^+\pi^-\pi^0\pi^0\eta$ Final State

The data set DAT-I (table 3.1) contains 5'832'973 triggered events. We collected it during 8 days of beam time with an average data acquisition rate of 17 Hz. After subtracting the time which was used to collect the calibration data sets (DAT-II, DAT-III, DAT-IV) one finds that the experiment was alive for 60% of the time. Reasons for the downtime were: spill breaks (refilling of LEAR), thunderstorms and some hardware problems.

### 4.1 Data Reduction

After reconstruction (section 3.2), real data and Monte Carlo events were run through an analysis program, which applied the cuts given in table 4.1. For the data sets DAT-I, DAT-III, DAT-IV, the first three entries which requested long tracks had almost no effect, because we had already asked for them in the trigger. In the data set DAT-I, 88% of the events had 2 well measured tracks with opposite charges.

The main tool of my data selection was the kinematic fit. It was important to use the correct errors  $\sigma_x$  on the measured quantities. For the kinematic fit to the four constraints

$$\begin{aligned}\sum_{i=1}^N \vec{P}_i &= 0 \\ \sum_{i=1}^N E_i &= 2m_p\end{aligned}\tag{4.1}$$

where N is the number of particles ( $8 \leq N \leq 10$ ), I used the minimum bias data set (DAT-II) to determine these errors. I scaled them until the gaussians which

Table 4.1: Data reduction for triggered real and Monte Carlo events (first two columnnes). In the last column, minimum bias data (no trigger) are shown. The trigger simulation was performed with 100% efficiency of the JDC accepting 12% of the events instead of 5% (Table 3.2) when including the JDC inefficiencies.

Event type Requirement	set DAT-I accepted	set MC-I accepted	set DAT-II accepted
total number of $\bar{p}$ (generated ev.)	-	$5.8 \cdot 10^6$	122'971
nr. of events after trigger (-simulation)	5'832'973	673'300	no trigger
all tracks start inside layer 5	5'793'892	668'500	110'282
all tracks contain at least 15 hits	5'515'785	654'500	44'143
two tracks with opposite charges	5'160'878	638'800	16'008
4C kinematic fit to total momentum and energy:			
after CBDROP confidence level $> 0.01$	3'643'580	549'400	5284
CBDROP found 6 photons	3'297'440	521'400	2253
7C kinematic fit:			
$\pi^0\pi^0\eta$ , confidence level $> 0.01$	580'349	444'600	165
$\pi^0\pi^0\pi^0$ & $\pi^0\eta\eta$ , confidence level $< 0.01$	495'038	437'200	138
only 1 comb. of $\pi^0\pi^0\eta$ , conf. level $> 0.2$	298'508	303'200	65
8C kinematic fit excluding $\omega, \eta \rightarrow \pi^+\pi^-\pi^0$ :			
$\omega \rightarrow \pi^+\pi^-\pi^0$ confidence level $< 0.01$	126'866	187'284	29
$\eta \rightarrow \pi^+\pi^-\pi^0$ confidence level $< 0.01$			

were fitted to the pulls (eq. 4.2) were centered at zero with a width of 1.0, and the confidence level distribution (which is the probability that the events satisfied equation 4.1) was flat. The pull was defined by

$$\text{pull} = \frac{x - x_{fit}}{\sqrt{\sigma_x^2 - \sigma_{fit}^2}} \quad (4.2)$$

with  $x$  and  $\sigma_x$  the measured quantities. These were for the JDC:  $\alpha$ , the curvature of the tracks in the transverse plane;  $\psi$ , the initial direction angle of the circle fit and  $\lambda$ , the slope of the track. With the calorimeter we measured  $\vartheta$ , the polar,  $\varphi$ , the azimuthal angle and the energy  $E$  of the photons.

Looking at the JDC  $z$ -distribution of the vertex (figure 2.3), one observes, that the  $\bar{p}$  stopped on average 0.17 cm upstream form the center of the detector. I also varied the  $z$ -vertex when fitting the momentum of the photons, and found a shift of -0.3 cm which is in nice agreement with observation. No correction was applied to the vertex coordinates perpendicular to the axis since the beam was

well aligned.

In spite of the vast recent improvements in the JDC tracking we still find that the momentum of the tracks is slightly too small and the discrepancy is different for positiv and negative charge. I therefore divided the transverse momentum by 1.023 for the negative and by 1.045 for the positive charge.

For all kinematic fits I used the 3 x 3 covariance matrix, including all the above corrections, which has the following form

$$\begin{pmatrix} \sigma_\alpha^2(2.1)^2 & \sigma_{\alpha\lambda}(2.1)(1.2) & \sigma_{\alpha\psi}(2.1)(1.1) \\ \sigma_{\lambda\alpha}(1.2)(2.1) & \sigma_\lambda^2(1.2)^2 & \sigma_{\lambda\psi}(1.2)(1.1) \\ \sigma_{\psi\alpha}(1.1)(2.1) & \sigma_{\psi\lambda}(1.1)(1.2) & \sigma_\psi^2(1.1)^2 \end{pmatrix} \quad (4.3)$$

for charged tracks, and

$$\begin{pmatrix} \sigma_\theta^2(1.3)^2 & \sigma_{\theta\phi}(1.3)(0.98) & \sigma_{\theta E}(1.3)(1.1) \\ \sigma_{\phi\theta}(0.98)(1.3) & \sigma_\phi^2(0.98)^2 & \sigma_{\phi E}(0.98)(1.1) \\ \sigma_{E\theta}(1.1)(1.3) & \sigma_{E\phi}(1.1)(0.98) & \sigma_E^2(1.1)^2 \end{pmatrix} \quad (4.4)$$

for photons. This led to the pulls and a confidence level distributions shown in figure 4.1.

The Monte Carlo data were produced with the vertex in the center of the barrel and therefore I used a centered vertex in the reconstruction and the kinematic fits. I did not correct the transverse momenta, but it was necessary to scale the errors, to get the pulls and the confidence levels correctly. The values used for charged tracks are:

$$\begin{pmatrix} \sigma_\alpha^2(1.4)^2 & \sigma_{\alpha\lambda}(1.4)(0.7) & \sigma_{\alpha\psi}(1.4)(1.2) \\ \sigma_{\lambda\alpha}(0.7)(1.4) & \sigma_\lambda^2(0.7)^2 & \sigma_{\lambda\psi}(0.7)(1.2) \\ \sigma_{\psi\alpha}(1.2)(1.4) & \sigma_{\psi\lambda}(1.2)(0.7) & \sigma_\psi^2(1.2)^2 \end{pmatrix} \quad (4.5)$$

and for photons:

$$\begin{pmatrix} \sigma_\theta^2(1.01)^2 & \sigma_{\theta\phi}(1.01)(0.82) & \sigma_{\theta E}(1.01)(1.01) \\ \sigma_{\phi\theta}(0.82)(1.01) & \sigma_\phi^2(0.82)^2 & \sigma_{\phi E}(0.82)(1.01) \\ \sigma_{E\theta}(1.01)(1.01) & \sigma_{E\phi}(1.01)(0.82) & \sigma_E^2(1.01)^2 \end{pmatrix}. \quad (4.6)$$

The algorithm CBDROP (described in section 3.2) was applied to clean the data sample. A fraction of 57% of all data events (set DAT-I) passed a confidence level cut of  $\geq 1\%$  and had exactly 6 photons, which demonstrates that the hardware trigger rejected background events with a high efficiency. For the minimum bias data set DAT-II the corresponding figure is only 1.8% (table 4.1)!

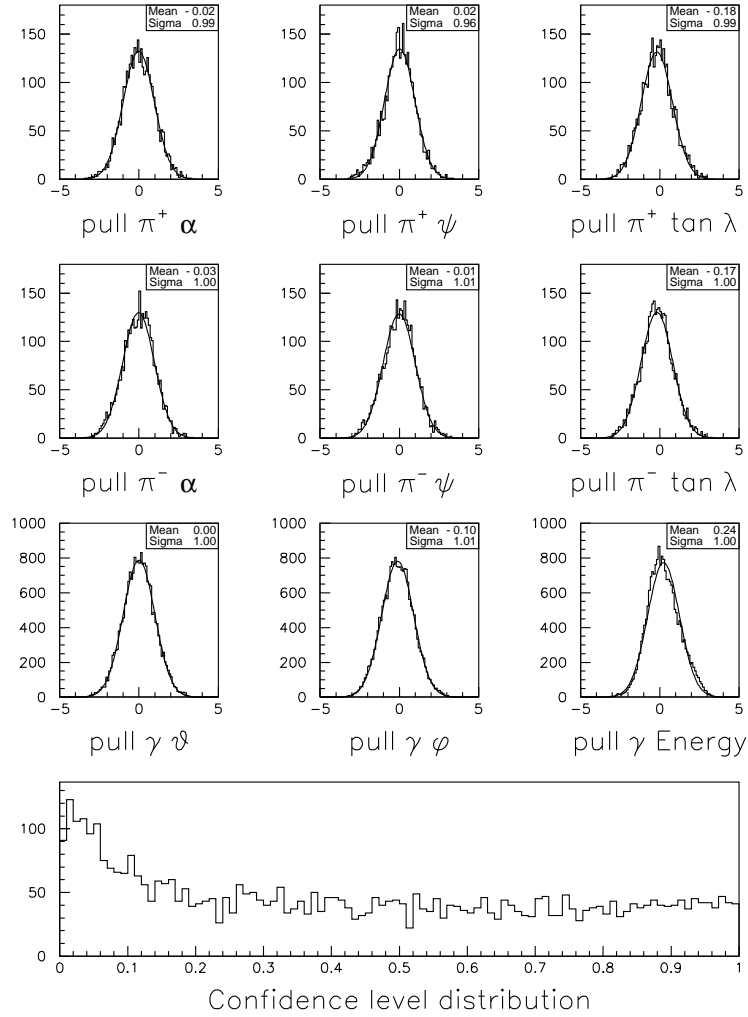


Figure 4.1: Pulls and confidence level distributions of the 4C kinematic fit for events with 2 long tracks in the minimum bias data sample (DAT-II).

With six photons one has 15 combinations to form 2  $\gamma$  invariant masses. They are plotted for a subset of the triggered data set DAT-I in figure 4.2a. The fit to a gaussian with a polynomial background found 135.7(6) MeV and  $\sigma=7.54(6)$  MeV for the  $\pi^0$  mass and width. The  $\eta$ -signal is somewhat distorted, because of the small misalignment of the trigger window due to uncertainties in the online energy calibration. Thus the values of 537.0(6) and  $\sigma=21.7(6)$  MeV are not very meaningful. The shift is also caused by the combinatorial background, which is larger on the left of the  $\eta$  signal than on the right, and therefore the trigger

accepted more background events (faked  $\eta$  events) on the left side.

I used the kinematic fit to determine which photon pairs arise from  $\pi^0$  or  $\eta$  decay. 7C fits were applied for all 15 combinations for each of the three final states  $\pi^+\pi^-3\pi^0$ ,  $\pi^+\pi^-2\pi^0\eta$  and  $\pi^+\pi^-\pi^02\eta$ . In order to accept an event I requested a confidence level of  $>20\%$  for the  $\pi^+\pi^-2\pi^0\eta$  hypothesis. If the fit still found a combination in one of the other two hypotheses with a confidence level  $>1\%$  the event was rejected. I tested the event selection with a simple algorithm, which chose the combination for which the sum of the deviations from the nominal meson masses weighted by the errors was minimum. All events with a sum smaller than 0.5 (which was found to be a reasonable limit) are compared with the result of the kinematic fit. They agree for 90% of the events. In order to test whether the 7C kinematic fit found the correct events, a 6C fit was applied with the constraints to total momentum, total energy and the mass of two  $\pi^0$ 's (figure 4.2b). The loss of 25% is mostly due to the 20% confidence level cut in the 7C fit. 94% of the events which are accepted by the 7C fit, have a  $2\gamma$  invariant mass in the  $\eta$  region for those 2 photons, which are not combined to a  $\pi^0$  by the 6C fit.

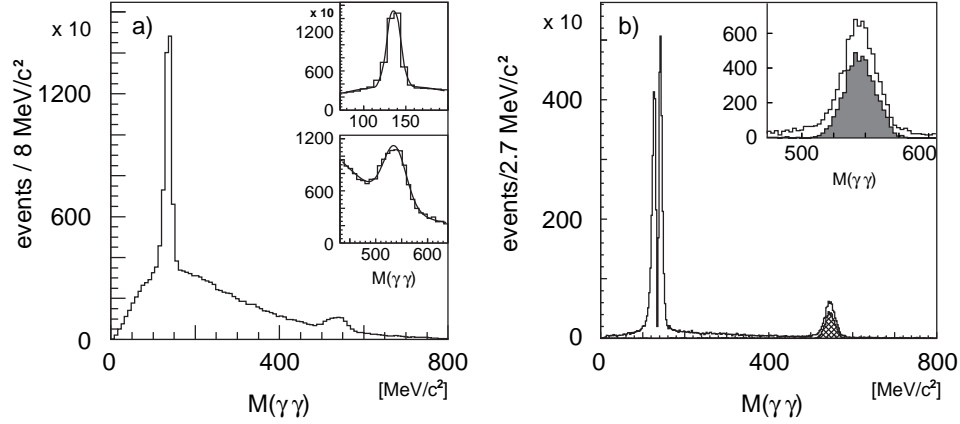


Figure 4.2: a) Invariant mass distribution (subset of DAT-I) for all (15) combinations of 2 photons. The insets show the  $\pi^0$  and  $\eta$  regions together with gaussian and polynomial fits.

b) Invariant ( $\gamma\gamma$ ) mass distribution of those two photons which are not found to be a  $\pi^0$  in the 6C kinematic fit to  $\pi^+\pi^-\pi^0\pi^0\gamma\gamma$ . The hole in the  $\pi^0$  peak is caused by the 6C fit, which accepts the combination with the two  $\pi^0$  closest to the nominal  $\pi^0$  mass (which are not plotted) for the  $\pi^+\pi^-3\pi^0$  final state. The hatched region contains those events, which are also accepted by the 7C fit with a confidence level  $>20\%$  to the  $2\pi^0\eta$  and  $<1\%$  to all other hypotheses.

To estimate the number of faked  $\eta$  by the trigger, I compared the number of events passing the 7C fit with a confidence level of 1% to the observed number of events in the peak before fitting (Fig 4.2a). The fraction of faked  $4\pi\eta$  events before the kinematic fit is therefore about 30%. These events are however removed by the 7C fit to  $4\pi\eta$ .

Ambiguous events with more than one  $2\pi^0\eta$  combination with a confidence level  $> 1\%$  are rejected, too. This cut may deplete certain regions of the phase space. Possible bias are however taken into account by submitting the Monte Carlo data to the same cuts.

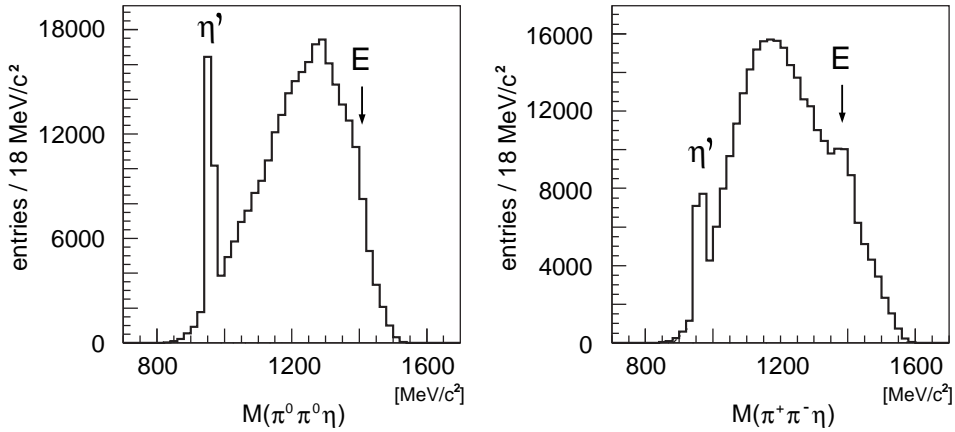


Figure 4.3: Invariant mass distributions of all  $\pi^+\pi^-\pi^0\pi^0\eta$  events.

I found 298'508 good  $\pi^+\pi^-\pi^0\pi^0\eta$  events, which is 5.1 % of the data on tape. The  $\eta\pi\pi$  mass distributions are shown in Figure 4.3. Apart from the strong  $\eta'$  signal one also observes a shoulder in the 1400 MeV region, presumably due to the E-meson.

Compared to the minimum bias data set DAT-II where one finds 0.06% reconstructable events, we achieved an enrichment of 97 (table 3.2). The average data acquisition rate for the trigger was 17 Hz (see figure 2.7) and 36 Hz for the minimum bias data. To get the same number of  $\pi^+\pi^-\pi^0\pi^0\eta$  events with the minimum bias trigger, one would therefore need a factor of 44 more time (352 days). As a cross check, I estimated the time which is needed to collect 300'000 reconstructable  $\pi^+\pi^-\pi^0\pi^0\eta$  events with information about the minimum bias data set only. Assuming also 60% lifetime of the experiment, as we had in case of the trigger, I find that we would need 322 days.

On the Monte Carlo data set MC-I I found that 5% of the events were ac-

cepted by the trigger (see table 3.2). A fraction of 45% were then accepted by the reconstruction as  $\pi^+\pi^-\pi^0\pi^0\eta$  events (Table 4.1) which led to an acceptance of 2.3%. Thus I found that the fraction of reconstructable  $\pi^+\pi^-\pi^0\pi^0\eta$  events accepted by the trigger was 24.7%.

## 4.2 The Final States $\omega\eta\pi^0$ and $\eta\eta\pi^0$

The most prominent signal in the data is  $\omega$  decay to  $\pi^+\pi^-\pi^0$  shown in figure 4.4b. The fit to a gaussian with a polynomial background gave an  $\omega$  mass of 783.9(1) which is slightly too high compared to the PDG value ( $m_\omega = 781.94 \pm 0.12$  MeV), and a experimental resolution of  $\sigma = 11.0(1)$  MeV. The recoiling  $\pi^0\eta$  system forms a strong resonance with a mass around 985 MeV and a width of approximately 50 MeV, which is the  $a_0(982)$  (figure 4.4a). This figure suggests that a large contribution stems from the annihilation channel  $\bar{p}p \rightarrow \omega a_0$ . An 8C kinematic fit to the  $\pi^0\eta\omega$  hypothesis was applied and found 131'370 events with a confidence level of more than 20%. The Dalitz plot of these events is shown in figure 4.5.

The same final state  $\pi^0\eta\omega$  but with  $\omega \rightarrow \pi^0\gamma$  [27] was measured by the Crystal Barrel experiment and it was shown in a detailed analysis that the contribution from  $\omega a_0$  is 52% of  $\pi^0\eta\omega$ . Our Dalitz plot (figure 4.5) is similar to the Dalitz plot obtained for  $\pi^0\eta\omega(\rightarrow \pi^0\gamma)$  [28]. In order to simplify the further analysis I removed all events which satisfy the  $\pi^0\eta\omega$  fit with a confidence level of more than

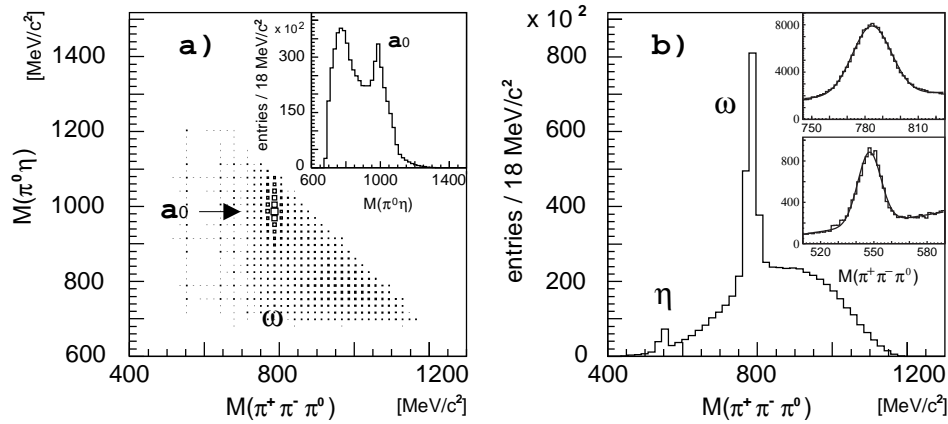


Figure 4.4: a)  $\pi^+\pi^-\pi^0$  vs.  $\pi^0\eta$  mass scatterplot (2 entries/event) of all  $\pi^+\pi^-\pi^0\pi^0\eta$  events (section 4.1) with  $\pi^0\eta$  mass projection (inset);  
 b)  $\pi^+\pi^-\pi^0$  invariant mass distribution The insets show the fits to  $\omega$  and  $\eta$  (gaussians with polynomial backgrounds).

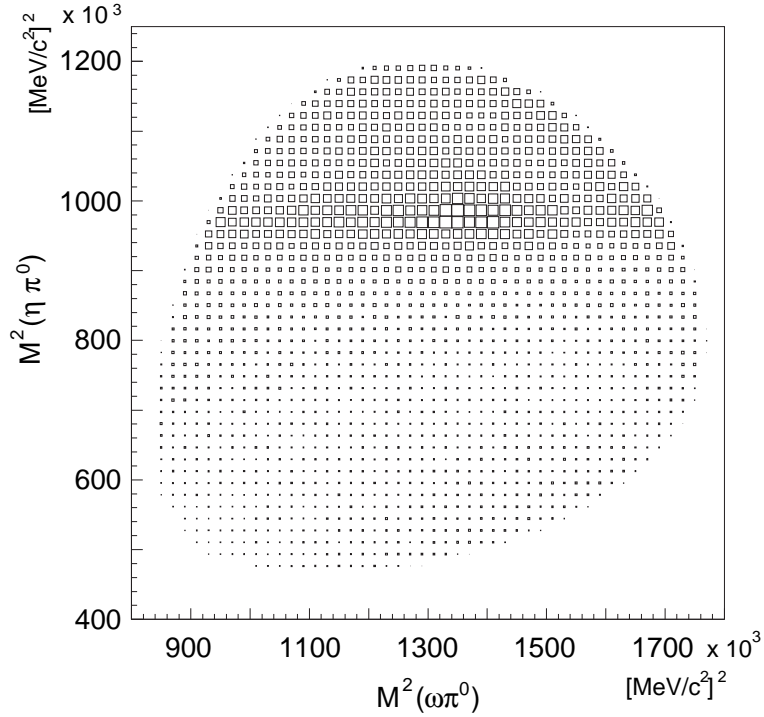


Figure 4.5: Dalitz plot of the  $\omega\eta\pi^0$  final state. The horizontal accumulation of events is due to  $a_0(980)$ .

1%. The fraction of  $\pi^0\eta\omega$  events is found to be  $\sim 57\%$  of the  $\pi^+\pi^-\pi^0\pi^0\eta$  data sample.

In the  $\pi^+\pi^-\pi^0$  invariant mass distribution (figure 4.4b) one also observes a small  $\eta$  signal. This is the  $\eta\eta\pi^0$  final state which was also studied previously by the Crystal Barrel experiment in the  $6\gamma$  final state [29]. The fit found an  $\eta$  mass of  $547.49(1)$  MeV and a width of  $\sigma=6.66(1)$  MeV. The fact that the  $\eta$  mass appears closer to the expected value ( $m_\eta = 547.45 \pm 0.19$  MeV), although the  $\omega$  is 2 MeV too high, points to small systematic effects in the scaling of the track momentum (see section 4.1). There are only a few events below the  $\eta$  signal, which means that we can safely remove the events which satisfy the 8C kinematic fit to the  $\eta\eta\pi^0$  hypothesis with more than 1%. This then leaves a sample of 126'866 events.

### 4.3 The $\eta\pi\pi$ Invariant Mass Distribution

In the  $\eta\pi\pi$  mass distributions (figure 4.6) one observes a strong  $\eta'$  signal and the expected enhancement in the  $E/\iota$  region. In order to study the  $E/\iota$  signal one would like to remove the  $\eta'$  signal, but in contrast to the  $\omega$  events which are

broadly distributed in the  $\eta\pi\pi$  histogram, the  $\eta'$  are enhanced in the region of 1400 MeV in the  $\eta\pi^+\pi^-$  invariant mass distribution for the  $\eta' \rightarrow \eta\pi^0\pi^0$  and in the  $\eta\pi^0\pi^0$  mass distribution for the  $\eta' \rightarrow \eta\pi^+\pi^-$ , as shown in the hatched regions of figure 4.6. These events produce reflections just below the  $E/\iota$  region and are therefore dangerous to remove.

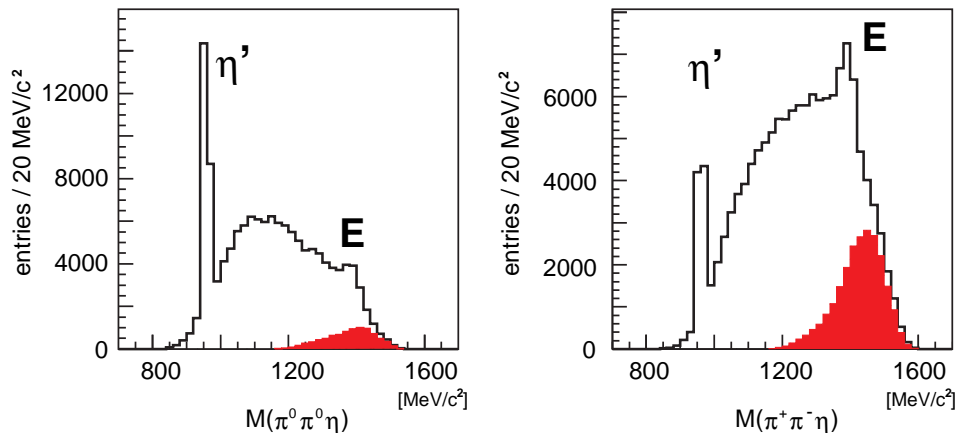


Figure 4.6: Invariant mass distributions of  $\pi^+\pi^-\pi^0\pi^0\eta$  events after removal of the  $\omega$  and  $\eta \rightarrow \pi^+\pi^-\pi^0$  contributions. The shaded regions are events with a  $\pi\pi\eta$  invariant mass between 937 and 977 MeV ( $\eta'$ ) from the crossed channels.

## 4.4 Final State Branching Ratios

An overview of the Monte Carlo data sets is given in table 4.2 A detection and reconstruction efficiency for  $\pi^+\pi^-(\pi^0\pi^0\eta \rightarrow 6\gamma)$  of 10.3(2)% (statistical error only) was derived for the minimum bias data set with the Monte Carlo data sample MC-I by submitting the events through the same analysis chain as real unbiased data (DAT-II). This seemingly low figure is mainly due to the long track requirement, which rejected approximately 60 % of the minimum bias events.

The most prominent background channel is the  $\pi^+\pi^-3\pi^0$  final state. A detection and reconstruction efficiency  $\epsilon_1$  for the  $\pi^+\pi^-3\pi^0$  Monte Carlo events (set MC-II) of 10.6(2)% was determined. From Monte Carlo simulations I found that the contamination of  $\pi^+\pi^-3\pi^0$  in the  $\pi^+\pi^-\pi^0\pi^0\eta$  final state is 3%.

Table 4.2: Overview about the Monte Carlo data sets (errors are statistical only).

- $\epsilon 1$ : 7C confidence level of its own hypothesis  $> 0.2$ , all other confidence levels  $< 0.01$   
 $\epsilon 2$ : trigger simulation (without JDC efficiency compare section 3.4) +  $\epsilon 1$  + only one combination of its own hypothesis with a confidence level  $> 0.01$

Nr.	Generated final state	total nr of generated events	nr events used to determine $\epsilon$	$\epsilon 1$	$\epsilon 2$
MC-I	$\pi^+\pi^-\pi^0\pi^0\eta \rightarrow \gamma\gamma$	$5.8 \times 10^6$	195000	10.3(2)%	2.30(3)%
MC-II	$\pi^+\pi^-\pi^0\pi^0\pi^0$	430'000	20000	10.6(2)%	
MC-III	$\omega\eta \rightarrow \gamma\gamma\pi^0$	15800	15800		2.3(2)%
MC-IV	$\eta\eta \rightarrow \gamma\gamma\pi^0$	3470	3470		1.8(1)%
MC-V	$\eta' \rightarrow \pi^0\pi^0\eta\pi^+\pi^-$	38100	38100		2.5(1)%

In the minimum bias data set DAT-II are 78  $\pi^+\pi^-\pi^0\pi^0\eta$  events<sup>1</sup> and 687  $\pi^+\pi^-3\pi^0$  events with a confidence level of more than 20% for their own hypothesis and  $< 1\%$  for all others. Subtracting the background from  $\pi^+\pi^-3\pi^0$  events satisfying the  $\pi^+\pi^-\pi^0\pi^0\eta$  hypotheses ( $3 \pm 1$  events) we are left with  $75 \pm 9$   $\pi^+\pi^-\pi^0\pi^0\eta$  events. Taking into account the detector and reconstruction efficiencies ( $\epsilon 1$  in table 4.2), the  $\eta \rightarrow \gamma\gamma$  branching ratio of 0.388(5) and the  $\pi^0 \rightarrow \gamma\gamma$  branching ratio of 0.988, I find a relative branching ratio of

$$\frac{B(\pi^+\pi^-\pi^0\pi^0\eta)}{B(\pi^+\pi^-3\pi^0)} = \frac{75}{687} \cdot \frac{\epsilon_1(\pi^+\pi^-\pi^0\pi^0\eta)}{\epsilon_1(\pi^+\pi^-3\pi^0)} \cdot \frac{B(\pi^0 \rightarrow \gamma\gamma)}{B(\eta \rightarrow \gamma\gamma)} = 0.270 \pm 0.035 \quad (4.7)$$

where the error is dominated by the statistical errors.

$\epsilon 1$  is the reconstruction efficiency for 100% JDC efficiency, a 7C confidence level of  $> 0.2$  and a confidence level  $< 0.01$  for the other channels (for instance  $\pi^+\pi^-\pi^0\pi^0\pi^0$  and  $\pi^+\pi^-\pi^0\eta\eta$  for the channel  $\pi^+\pi^-\pi^0\pi^0\eta$ ).  $\epsilon 2$  is the reconstruction efficiency with the trigger simulation (hence the correct JDC efficiency see table 3.2), a 7C confidence level  $> 0.2$ , a confidence level  $< 0.01$  for the other hypotheses and only one combination of its own hypothesis with a confidence level  $> 0.01$ .

I then used the branching ratio for  $\pi^+\pi^-3\pi^0$  which was measured by the Crystal Barrel experiment [30] to be  $(97 \pm 6) \cdot 10^{-3}$  (where the error is mainly systematic). This leads to the absolute branching ratio of  $\text{BR}(\bar{p}p \rightarrow \pi^+\pi^-\pi^0\pi^0\eta) = 26.2 \pm 3.7 \cdot 10^{-3}$ .

<sup>1</sup>The requirement to accept only events which have exactly one 7C  $\pi^+\pi^-\pi^0\pi^0\eta$  fit combination with a confidence level above 1%, is not applied here; this increases the number of events from 65 (Table 4.1) to 78

Table 4.3: Branching ratios for  $\pi^+\pi^-\pi^0\pi^0\eta$  using known branching ratios from other experiments.

final state X	branching ratio	ref	$\pi^+\pi^-\pi^0\pi^0\eta$ branching ratio
$\pi^+\pi^-\pi^0\pi^0\pi^0$	$9.7\pm 0.6\%$	[30]	$2.62\pm 0.37\%$
$\omega\eta\pi^0$	$0.68\pm 0.01\pm 0.05\%$	[27]	$1.78\pm 0.21\%$
$\eta\eta\pi^0$	$0.21\pm 0.04\%$	[29]	$3.24\pm 0.65\%$
$\eta'\pi^+\pi^-$	$0.35\pm 0.07\%$	[31]	$1.12 \pm 0.23\%$

This branching ratio can also be determined by the known  $\omega\eta\pi^0$ ,  $\eta\eta\pi^0$  and  $\eta'\pi^+\pi^-$  branching ratios. The data set DAT-II is however not large enough and therefore I used the triggered data DAT-I. The fit to a gaussian and a polynomial background shown in the inset of figure 4.2a found  $N(\omega\eta\pi^0)=101'520\pm 1440$  events. To determine the  $\pi^+\pi^-\pi^0\pi^0\eta$  branching ratio I used the following equation:

$$B(\pi^+\pi^-\pi^0\pi^0\eta) = \frac{N(\pi^+\pi^-\pi^0\pi^0\eta)}{N(\omega\eta\pi^0)} * \frac{\epsilon_2(\omega\eta\pi^0)}{\epsilon_2(\pi^+\pi^-\pi^0\pi^0\eta)} * B(\omega\eta\pi^0) * B(\omega \rightarrow \pi^+\pi^-\pi^0) \quad (4.8)$$

where  $\epsilon_2$  are the trigger, detector and reconstruction efficiencies (table 4.2). Using the branching ratio for  $\omega\eta\pi^0$  from [27] (table 4.3)  $B(\omega \rightarrow \pi^+\pi^-\pi^0) = 88.8\pm 0.7\%$  and  $N(\pi^+\pi^-\pi^0\pi^0\eta) = 298508\pm 546$  (table 4.1) I then found  $B(\pi^+\pi^-\pi^0\pi^0\eta) = 1.78\pm 0.21\%$ , where the error is dominated by the error on  $\epsilon_2$  and the systematic error of the  $\omega\eta\pi^0$  branching ratio.

The same procedure can be applied for  $\eta\eta\pi^0$  where I found  $7155 \pm 253$  events and  $\eta'\pi^+\pi^-$  ( $21142 \pm 383$  events) for which we know the branching ratios. There are two possible combinations for each  $\eta$  decay and therefore the branching ratio for  $B(\eta\eta\pi^0)$  must be multiplied by two. Using  $B(\eta \rightarrow \pi^+\pi^-\pi^0) = 23.6\pm 0.6\%$  and  $B(\eta' \rightarrow \pi^0\pi^0\eta) = 20.8\pm 1.5\%$  I obtain the results given in table 4.3.

The values obtained by the  $\eta'\pi^+\pi^-$  in the ASTERIX experiment [31] are not compatible with the other three branching ratios from Crystal Barrel. I still average the four results using the Rosenfeld method:

$$\bar{b} = \frac{\sum_{i=1}^4 \frac{b_i}{\sigma_i^2}}{\frac{1}{\bar{\sigma}^2}} \quad (4.9)$$

$$\bar{\sigma} = \sqrt{\frac{1}{\sum_{i=1}^4 \frac{1}{\sigma_i^2}}}$$

where  $b_i$  are the branching ratios. This leads to

$$\chi^2 = \sum_{i=1}^4 \frac{(\bar{b} - b_i)^2}{\sigma_i^2} = 18.3 \quad (4.10)$$

for 3 degrees of freedom. I then increase the errors  $\sigma_i^2$  to obtain a  $\chi^2$  of 3 and find

$$B(\pi^+\pi^-\pi^0\pi^0\eta) = 1.72 \pm 0.34\%. \quad (4.11)$$

Using instead only the first 3 measurements I find

$$B(\pi^+\pi^-\pi^0\pi^0\eta) = 2.08 \pm 0.34\%. \quad (4.12)$$

This is the value I will use for the further discussion.

## 4.5 The $\pi^+\pi^-\pi^0\eta\eta$ Final State

We allowed the trigger to accept  $\pi^+\pi^-\pi^0\eta\eta$  events too (section 2.2.2), by setting the maximum number of  $\eta$  in the software trigger to 2. The same data reduction as for the  $\pi^+\pi^-\pi^0\pi^0\eta$  final state was applied (with adapted hypotheses for the kinematic fit of course) and I found a sample of 1474 reconstructed  $\pi^+\pi^-\pi^0\eta\eta$  events. The  $\pi^+\pi^-\pi^0$  invariant mass distribution is plotted in the lower inset of figure 4.7. A clear peak shows approximately 800  $\eta\eta\eta$  events. Removing them I get the  $\pi^+\pi^-\eta$  invariant mass distribution shown in the upper inset of figure 4.7 with a prominent  $\eta'$  signal. Using the events in this peak (e.g. using events with  $938 \text{ MeV} < M(\pi^+\pi^-\eta) < 978 \text{ MeV}$ ) one finds for the  $\eta\eta'\pi^0$  final state 311 events plotted in figures 4.7 and 4.8a.

The final state  $\pi^0\eta\eta'$  was already studied by the Crystal Barrel where the  $\eta'$  decays into  $\gamma\gamma$  [32]. The  $\eta\eta'$  threshold enhancement (figure 4.8b) is due to the new state  $f_0(1500) \rightarrow \eta\eta'$ . It is gratifying that  $\pi^+\pi^-\pi^0\pi^0\eta$  reproduces the resonance behaviour of the  $\eta\eta'$  system in a final state with entirely different experimental systematics. Because my sample is relatively small and the background more difficult to understand the fit was not repeated.

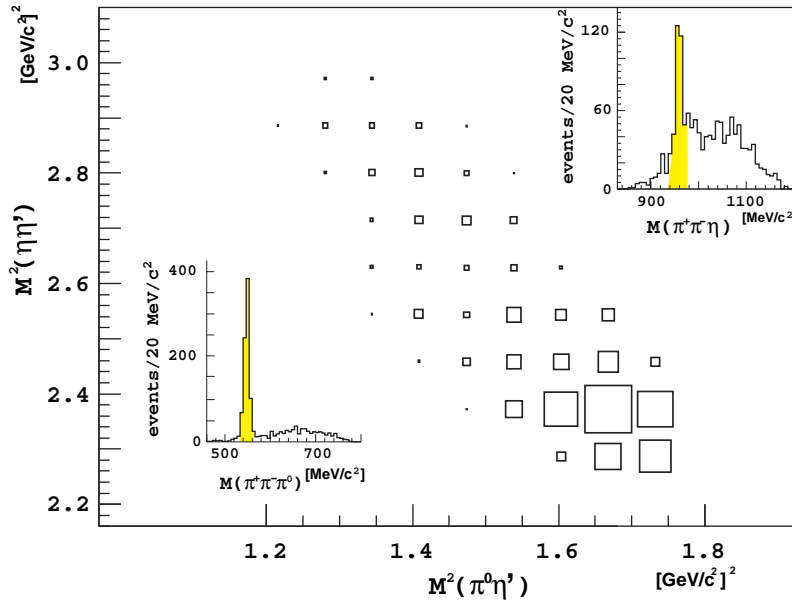


Figure 4.7: Dalitz plot for the  $\eta\eta'\pi^0$  channel from the  $\pi^+\pi^-\pi^0\eta\eta$  final state. The insets show the  $\pi^+\pi^-\pi^0$  and the  $\pi^+\pi^-\eta$  invariant mass distributions (2 entries per event) with the cuts used to select the  $\eta'$  events.

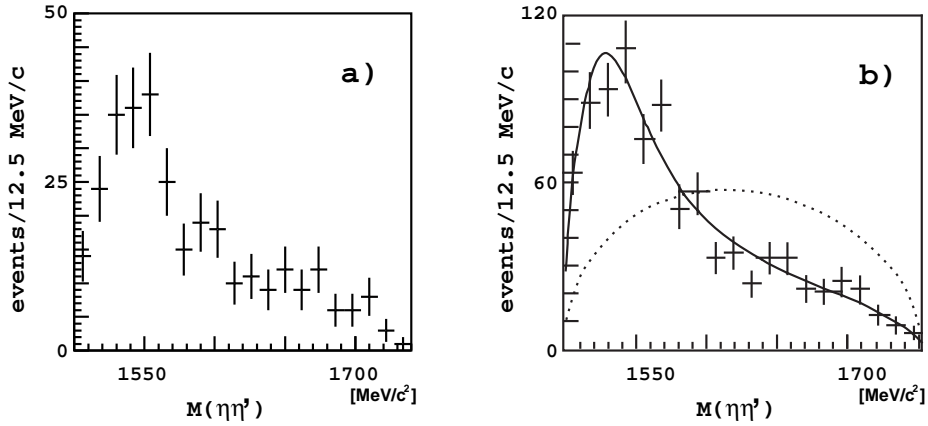


Figure 4.8: The  $\eta\eta'$  invariant mass spectrum shows the same resonance behaviour for the  $\pi^0\eta(\eta' \rightarrow \pi^+\pi^-\eta)$  a) and the  $\pi^0\eta(\eta' \rightarrow \gamma\gamma)$  final states b). The full line is the fit found in [32], the dotted line shows pure phase space.



# Chapter 5

## Discussion

### 5.1 Spin-Parity Analysis

#### 5.1.1 Transition Probability

The  $\pi^+\pi^-\pi^0\pi^0\eta$  data were analyzed using a maximum likelihood fit. The analysis was done in the helicity formalism [33] in terms of the isobar model [34], in which the initial  $\bar{p}p$  system is assumed to decay to the  $\pi^+\pi^-\pi^0\pi^0\eta$  final state through two-body intermediate states. The decay chain is assumed to be a succession of two-body decays of the following forms:

$$\begin{aligned} \bar{p}p &\rightarrow AB, & A &\rightarrow C\eta, & B &\rightarrow \pi\pi, & C &\rightarrow \pi\pi & (5.1) \\ &or & A &\rightarrow C\pi, & B &\rightarrow \pi\pi, & C &\rightarrow \eta\pi \\ or & \bar{p}p &\rightarrow A\eta & & A &\rightarrow CD & & C &\rightarrow \pi\pi, & D &\rightarrow \pi\pi \end{aligned}$$

The procedure is to fit the different combinations of decay chains given in table 5.1. The various chains are added coherently if they have the same initial state  $^1S_0$  or  $^3S_1$ . The fit determines the contribution of each hypothesis. In the helicity formalism, an isobar of spin  $J$  decays into two daughters of spin  $S_1$  and  $S_2$ . The daughters have total spin  $S$  and relative angular momentum  $L$ . The decay amplitude is given by the matrix  $A$ :

$$A(J; LS) = D_{\lambda M}^J(\theta, \phi) \langle J\lambda | LS0\lambda \rangle \langle S\lambda | S_1 S_2 \lambda_1, -\lambda_2 \rangle \times F_L(q) \times BW_L(m). \quad (5.2)$$

The row index  $\lambda = \lambda_1 - \lambda_2$  runs over the  $(2S_1 + 1)(2S_2 + 1)$  final states helicities, while the column index  $M$  runs over the  $(2J + 1)$  magnetic substates of the isobar;  $q$  is the final state momentum and  $\theta$  and  $\phi$  refer to the decay angles in the isobar rest frame. The amplitude of a whole chain is the product of the matrices of the

individual decays [35].  $BW_L(m)$  is the Breit-Wigner amplitude (defined below) for the mass  $m$  of the isobar, and  $F_L$  are the Blatt-Weisskopf damping factors [36] which are needed to take into account the suppression of higher angular momenta. They are given by:

$$\begin{aligned} F_0(q) &= 1 \\ F_1(q) &= \sqrt{\frac{2z}{z+1}} \\ F_2(q) &= \sqrt{\frac{13z^2}{(z-3)^2 + 9z}} \end{aligned} \quad (5.3)$$

where  $z = \left(\frac{q[M\epsilon V]/c}{197.3}\right)^2$ . The Breit-Wigner factors are given by

$$BW_L(m) = \frac{m_0 \Gamma_0}{m_0^2 - m^2 - im_0 \Gamma(m)}, \quad (5.4)$$

where

$$\Gamma(m) = \Gamma_0 \frac{m_0}{m} \frac{q}{q_0} \frac{F_L^2(q)}{F_L^2(q_0)}, \quad (5.5)$$

with  $m_0$  and  $\Gamma_0$  the nominal mass and width of the resonance and  $q_0$  the corresponding decay momentum. For the initial  $\bar{p}p$  system  $BW=1$ . For a state decaying into two broad resonances (e.g.  $f_0(1400) \rightarrow \rho\rho$ ) the daughter momentum  $q_0$  becomes imaginary if it is computed using the nominal masses (since  $f_0(1400)$  is below  $\rho\rho$  threshold). To avoid this problem I use the low mass limit, which is the sum of the masses of the daughters (e.g.  $4m_\pi$ ) [37].

For the  $\pi\pi$  S-wave I use the parametrisation  $K_1$  from reference [38] in terms of the S-wave shift  $\delta$  and the inelasticity  $\eta$  which was measured in elastic  $\pi\pi$  scattering. I replace the Breit-Wigner amplitude as a function of the  $\pi^0\pi^0$  or  $\pi^+\pi^-$  invariant mass by

$$BW_{L=0}(m_{\pi\pi}) = \frac{m_{\pi\pi}}{q} \left\{ \frac{\eta(m_{\pi\pi}) e^{2i\delta(m_{\pi\pi})} - 1}{2i} \right\}. \quad (5.6)$$

I assumed S-state annihilation dominance in liquid hydrogen [39] and used therefore only contributions from the S-states of the  $\bar{p}p$  system to  $\pi^+\pi^-\pi^0\pi^0\eta$ :  $^1S_0[I^G(J^{PC}) = 0^+(0^{-+})]$  and  $^3S_1[I^G(J^{PC}) = 1^+(1^{-})]$ . The transition probability  $w$  for an event  $j$  is given by the following sum:

$$w_j = w_{PS} \left[ \text{tr} \left| \sum_{l_1=1}^{L_1} \alpha_{l_1} A_{l_1}({}^1S_0) \right|^2 + \text{tr} \left\{ \left( \sum_{l_2=1}^{L_2} \alpha_{l_2} A_{l_2}({}^3S_1) \right) \cdot \rho \cdot \left( \sum_{l_2=1}^{L_2} \alpha_{l_2} A_{l_2}({}^3S_1) \right)^+ \right\} \right] \quad (5.7)$$

where  $w_{PS}$  is the phase space weight,  $\alpha_{l_k} = a_{l_k} e^{i\phi_{l_k}}$  are unknown constants,  $L_1$ ,  $L_2$  are the number of decay chains,  $A_{l_i}$  is the decay amplitude of chain  $l_i$  and  $\rho$  is the density matrix of the  ${}^3S_1$  initial state:

$$\rho = \begin{pmatrix} \frac{1}{3} & 0 & 0 \\ 0 & \frac{1}{3} & 0 \\ 0 & 0 & \frac{1}{3} \end{pmatrix} \quad (5.8)$$

### 5.1.2 Maximum Likelihood Fit

Events with 5 particles in the final state are kinematically described with  $3 \times 5$  variables from which one subtracts 4 degrees of freedom due to conservation of total energy and momentum and another 3 Euler angles because the orientation of the system is arbitrary. We are then left with 8 independent variables. Thus it is impossible to fit the data in binned histograms (assuming 10 bins per variable one would get  $10^8$  bins!). Therefore I use the maximum likelihood method which fits individual events.

For every event the transition probability  $w$  (eq. 5.7) behaves as a probability density, if one normalizes the individual probabilities by the integral over phase space.

$$w_j \rightarrow \frac{w_j}{\sum_{i=1}^M w'_i}, \quad (5.9)$$

where  $w'$  is the weight of Monte Carlo events according to 5.7 and  $M$  is the number of Monte Carlo events. The definition of the standard likelihood which needs to be maximized is

$$L = \prod_{j=1}^N \frac{w_j}{\sum_{i=1}^M w_i} \quad (5.10)$$

with  $N$  the number of data events. Since the product consists of many small

numbers I minimized the negative logarithm:

$$-\ln L = N \ln \left( \sum_{i=1}^M w_i \right) - \sum_{j=1}^N \ln w_j. \quad (5.11)$$

To normalize the Monte Carlo data to the real data one should renormalize the  $w_j$  and  $w'_j$ , by replacing

$$w_j, w'_j \rightarrow \frac{w_j, w'_j}{\sum_{i=1}^M |A_i|^2} \quad (5.12)$$

or equivalently

$$A_{jl} \rightarrow \frac{A_{jl}}{\sqrt{\sum_{i=1}^M |A_{jl}|^2}} \quad (5.13)$$

for every event of both the real and the Monte Carlo data sets separately for each  $\bar{p}p$  initial state.

The fits were done with fixed masses and resonances. Therefore the renormalized amplitudes  $A_{jl}$  (eq. 5.13) which do not contain any free parameters, for each real event  $j$  and each decay chain  $l$  was calculated and stored before starting the minimization procedure. Thus in each iteration (adjusting  $a_l$  and  $\phi_l$ ) the fit program had only to calculate:

$$W_{dat} = \sum_{j=1}^N \ln \left[ \text{tr} \left| \sum_{l=1}^{L_1} a_l e^{-i\phi_l} A_{jl}({}^1S_0) \right|^2 + \text{tr} \left\{ \left( \sum_{l=1}^{L_2} a_l e^{-i\phi_l} A_{jl}({}^3S_1) \right) \cdot \rho \cdot \left( \sum_{l=1}^{L_2} a_l e^{-i\phi_l} A_{jl}({}^3S_1) \right)^+ \right\} \right] \quad (5.14)$$

The calculation of the normalization factor can be done similarly. The performance of the program was increased by replacing (separately for  ${}^1S_0$  and  ${}^3S_1$   $\bar{p}p$  initial states)  $\sum_{i=1}^M w_i$  (eq. 5.11) with

$$W_{MC} = \sum_{l=1}^L a_l^2 + \sum_{l < m} 2a_l a_m P_R^{lm} \cos(\phi_m - \phi_l) + \sum_{l < m} 2a_l a_m P_I^{lm} \sin(\phi_m - \phi_l) \quad (5.15)$$

where  $m$  runs from 1 to the number of decay chains  $L$  of the specified initial state and

$$P_R^{lm} = \frac{\sum_{i=1}^M \Re(A_{li}^+ A_{mi})}{\sqrt{\sum_{i=1}^M |A_{li}|^2} \sqrt{\sum_{i=1}^M |A_{mi}|^2}} \quad (5.16)$$

$$P_I^{lm} = \frac{\sum_{i=1}^M \Im(A_{li}^+ A_{mi})}{\sqrt{\sum_{i=1}^M |A_{li}|^2} \sqrt{\sum_{i=1}^M |A_{mi}|^2}}.$$

Finally the minimized quantity was according to eq. 5.11

$$S = \chi^2 = -2 \cdot \ln L = 2 \cdot N \cdot \ln \left( W_{\text{MC}}(^1S_0) + W_{\text{MC}}(^3S_1) \right) - 2 \cdot W_{\text{dat}} \quad (5.17)$$

The factor 2 allows the minimization of a  $\chi^2$  using standard routines (e.g. MINUIT) providing the correct errors  $\sigma$ . The relative contribution of each amplitude from chain  $l$  is given by

$$a_l \rightarrow \frac{a_l}{\sqrt{\sum_{i=1}^{N_l} a_i^2}}. \quad (5.18)$$

where the sum extends over all chains ( $^3S_1$  and  $^1S_0$ ). For each initial state the phase  $\phi$  of one decay chain is arbitrary and set to 0.

### 5.1.3 Overview about Resonances and Decay Chains

In order to fit the  $E/\nu$  it was necessary to find a description of the “background” decay chains which do not contribute to the  $E/\nu$  signal. In addition to chains which consist only of two particle decays I used direct contributions. By direct contribution I mean  $\bar{p}p \rightarrow \text{ABC}$  conserving angular momentum and parity but with infinite resonance widths.

The various chains are listed in table 5.1.  $X(0^{++})$  in chains 1 and 2 are direct contributions decaying to  $(\pi^+\pi^-)_s(\pi^0\pi^0)_s$  and  $\rho(\pi^0\pi^0)_s$ , where the 2 dipion state is simulated as a  $(0^{++})$  state with a Breit-Wigner of infinite width. For  $\eta' \rightarrow \eta\pi\pi$  (chains 3, 8 and 22) I used 3-body phase space since the  $\eta'$  decay Dalitz plot is, to a very good approximation entirely flat [40]. This also agrees with other Crystal Barrel measurements. The  $X_2$  in chain 8 is the  $a_2(1650)$  reported by the Crystal Barrel [41]. The  $f_0(1365)$  in chains 9 and 10 is the  $f_0(1365)$  found by the Crystal Barrel decaying to  $\rho\rho$  or two pairs of pions  $(\pi\pi)_s$  in a relative S-wave [30].  $X(1^{--})$  in chains 20 and 21,  $X(1^{-+})$  in chains 23 and 24 and  $X(0^{-+})$  in chains 25 and 26 are further direct contributions. I have neglected contributions from channels with  $\pi\pi$  in a relative D wave (e.g.  $f_2(1270)$ ) and  $\pi\eta$  in a relative D wave (e.g.  $a_2(1320)$ ). This is justified by the lack of phase space for these reactions at rest.

Sometimes one finds two possibilities to form a specific decay chain, for example due to the fact that we have  $2\pi^0$  (e.g.  $E/\nu \rightarrow \pi_1^0 a_0^0 (\rightarrow \pi_2^0 \eta)$  and  $E/\nu \rightarrow \pi_2^0 a_0^0 (\rightarrow \pi_1^0 \eta)$ ). I took the sum of the two corresponding chains and used only one set of fit parameters ( $a_l, \phi_l$ ). In table 5.1 the last column shows the total number of chains of the indicated type.

My program cannot fit masses and widths. It would consume too much time, because it would have to calculate the amplitudes for all events in each iteration.

Table 5.1: Intermediate states considered in this analysis.  $I$  is the initial  $\bar{p}p$  atomic state,  $L$  is the relative orbital angular momentum, and  $S$  the total spin of the  $\bar{p}p \rightarrow AB$  system.  $l$  and  $s$  refer to the  $A \rightarrow CD$  system and  $nr$  are the number of possible contributions (symmetry or different charges).

	$I$	$\bar{p} \rightarrow A B$	$L$	$S$	$A \rightarrow C D$	$l$	$s$	$nr$
1	$^1S_0$	$X(0^{++}) \eta$	0	0	$(\pi^+\pi^-)_s (\pi^0\pi^0)_s$	0	0	1
2	$^1S_0$	$X(0^{++}) \eta$	0	0	$\rho^+ \rho^-$	0	0	2
3	$^1S_0$	$\eta' (\pi\pi)_s$	0	0	$\pi\pi \eta$	0	0	2
4	$^1S_0$	$E/\iota(0^{-+}) (\pi\pi)_s$	0	0	$(\pi\pi)_s \eta$	0	0	2
5	$^1S_0$	$E/\iota(0^{-+}) (\pi\pi)_s$	0	0	$\pi (a_0 \rightarrow \pi\eta)$	0	0	4
6	$^1S_0$	$E/\iota(1^{++}) (\pi\pi)_s$	1	1	$(\pi\pi)_s \eta$	1	0	2
7	$^1S_0$	$E/\iota(1^{++}) (\pi\pi)_s$	1	1	$\pi (a_0 \rightarrow \pi\eta)$	1	0	4
8	$^1S_0$	$X_2(2^{++}) \pi$	2	2	$\pi \eta' \rightarrow \pi\pi\eta$	2	0	4
9	$^1S_0$	$f_0(1365)(0^{++}) \eta$	0	0	$(\pi^+\pi^-)_s (\pi^0\pi^0)_s$	0	0	1
10	$^1S_0$	$f_0(1365)(0^{++}) \eta$	0	0	$\rho^+ \rho^-$	0	0	2
11	$^1S_0$	$\eta(1295)(0^{-+}) (\pi\pi)_s$	0	0	$(\pi\pi)_s \eta$	0	0	2
12	$^1S_0$	$\eta(1295)(0^{-+}) (\pi\pi)_s$	0	0	$\pi (a_0 \rightarrow \pi\eta)$	0	0	4
20	$^3S_1$	$X(1^{--}) \eta$	1	1	$\rho^0 (\pi^0\pi^0)_s$	0,2	1	2
21	$^3S_1$	$X(1^{--}) (\pi^0\pi^0)_s$	0	1	$\eta \rho^0$	1	1	1
22	$^3S_1$	$\eta' \rho^0$	1	1	$\pi^0\pi^0 \eta$	0	0	1
23	$^3S_1$	$X(1^{+-}) (\pi^0\pi^0)_s$	1	1	$\eta \rho^0$	0	1	1
24	$^3S_1$	$X(1^{+-}) (\pi^0\pi^0)_s$	1	1	$\pi a_0 \rightarrow \pi\eta$	1	0	2
25	$^3S_1$	$X(0^{-+}) \rho^0$	1	1	$(\pi^0\pi^0)_s \eta$	0	0	1
26	$^3S_1$	$X(0^{-+}) \rho^0$	1	1	$\pi^0 (a_0 \rightarrow \pi^0\eta)$	0	0	2
27	$^3S_1$	$E/\iota(0^{-+}) \rho^0$	1	1	$(\pi^0\pi^0)_s \eta$	0	0	1
28	$^3S_1$	$E/\iota(0^{-+}) \rho^0$	1	1	$\pi^0 (a_0 \rightarrow \pi^0\eta)$	0	0	2
29	$^3S_1$	$\rho(1400)(1^{--}) (\pi^0\pi^0)_s$	0	1	$\eta \rho^0$	1	1	1
30	$^3S_1$	$\rho(1400)(1^{--}) \eta$	1	1	$\rho^0 (\pi^0\pi^0)_s$	0,2	1	2
31	$^3S_1$	$b_1(1235)(1^{+-}) (\pi^0\pi^0)_s$	1	1	$\rho^0 \eta$	0	1	1
32	$^3S_1$	$b_1(1235)(1^{+-}) (\pi^0\pi^0)_s$	1	1	$\pi a_0 \rightarrow \pi\eta$	1	0	2

I estimated that the time for an optimized program on our fastest machine (IBM RISC 6000) would be more than a 100 hours per fit (with 20 chains). Instead I repeated some of the fits by changing the mass and widths within reasonable limits.

## 5.2 Results

### 5.2.1 General Features

In a first step I neglected the comparatively small  $E/\iota$  signal and determined the chains which contribute to the background. A first attempt was to use only the direct contributions (chain 1,2 and 20 in table 5.1). This results in a  $S = -2 \cdot \ln(L)$  of 2'984'862. Adding the  $(\pi\pi)_s\eta'$  and  $(\rho^0\eta')$  contributions (chains 3 and 22) where the  $\eta'$  decays directly into  $\pi\pi\eta$ , I found a reduction of  $\Delta S = 68965$  (11494 per free parameter) where  $\Delta S = 2 \Delta \ln L$ .

The  $\eta'$  is simulated with a gaussian, because the width of the signal is caused by the resolution of the detector. The phase space distribution is very low in the  $\eta'$  region. Because the  $\eta'$  is a huge signal in the data, the Monte Carlo events located in the region of the  $\eta'$  in the phase space get a large weight and a large error on the fitted  $\eta'$  signal, due to the low Monte Carlo statistics in the  $\eta'$ .

Five further direct contributions were then introduced to describe the background:

The channel  ${}^3S_1 \rightarrow (\pi^0\pi^0)_s X(1^{--})$  (chain 21) caused a reduction of 716.

The channel  ${}^3S_1 \rightarrow (\pi^0\pi^0)_s X(1^{+-})$  where the  $X(1^{+-})$  decays either to  $\rho^0\eta$  (chain 23) (the reduction of  $S$  is 1501), or into  $a_0^\pm \pi^\mp$  (chain 24) with a reduction of 1445.

The channel  ${}^3S_1 \rightarrow \rho^0 X(0^{-+})$  (chains 25, 26), where the  $X(0^{-+})$  decays to  $(\pi^0\pi^0)_s\eta$  and to  $a_0\pi$ , reduced  $S$  by 2977.

This led to a reasonable but not perfect description of the “background”. The intensities are given in table 5.2 (hypothesis A). The channels listed in table 5.1 but not in table 5.2 led to negligible contributions.

### 5.2.2 $E/\iota$ Fit

I then introduced  $\bar{p}p \rightarrow (\pi\pi)_s E/\iota(0^{-+})$  where  $E$  decays to (i)  $(\pi\pi)_s\eta$  (chain 4), (ii)  $a_0\pi$  (chain 5). I found a reduction of 8109 of  $S$  compared to fit A. The intensities of this best fit and their errors are listed in table 5.2 hypothesis B. The errors are taken into account by using the full covariance matrix.

Figure 5.1 shows the 2-dimensional projection of  $\pi\pi\eta$  versus  $\pi\pi$  masses. For visualisation purpose the  $E$  region, marked by an arrow, is projected on the  $x$ -axis, by restricting the  $(\pi\pi)$  mass recoiling against  $E$  to below 520 MeV, and shown in figure 5.2. In order to estimate what fraction is “background” I plotted the fit result A (without the  $E/\iota$  channel). Fit A alone, clearly does not describe the  $E$  region correctly. Estimating the number of  $E/\iota$  from this plot is misleading,

Table 5.2: Fit Results

The chains are described in detail in table 5.1; here  $\sigma$  means  $(\pi\pi)_s$ . The intensities are given as fractional contributions to the final state  $\pi^+\pi^-\pi^0\pi^0\eta$  (with  $\omega\eta\pi$  and  $\eta\eta\pi$  contributions removed) by squaring the amplitudes  $a_j$ .

Fit A: background only.

Fit B: fit A including the  $0^{-+}$  E/ $\iota$  signal.

Fit C: fit A including a  $1^{++}$  E/ $\iota$  signal.

Fit D: fit A including both  $0^{-+}$  and  $1^{++}$  contributions.

Fit E: fit B with  $\eta'$  events removed in data, the intensities are normalized to the data set including  $\eta'$  and therefore directly comparable to fit B.

	fit A	fit B	fit C	fit D	fit E
Likelihood S:	2'909'258	2'901'149	2'907'814	2'901'010	2'206'738
chain	intensity	intensity	intensity	intensity	intensity
1 X(0 <sup>++</sup> ) $\rightarrow$ $\sigma^0\sigma^{+-}$	0.152	0.093 $\pm$ 0.007	0.163	0.078	0.091
2 X(0 <sup>++</sup> ) $\rightarrow$ $\rho^+\rho^-$	0.291	0.289 $\pm$ 0.013	0.382	0.277	0.268
3 $\sigma^0(\eta' \rightarrow \pi^+\pi^-\eta)$	0.041	0.041 $\pm$ 0.005	0.052	0.039	
$\sigma^{+-}(\eta' \rightarrow \pi^0\pi^0\eta)$	0.087	0.091 $\pm$ 0.007	0.117	0.104	
4 E(0 <sup>-+</sup> ) $\rightarrow$ $\eta\sigma^0$		0.020 $\pm$ 0.003		0.018	0.020
E(0 <sup>-+</sup> ) $\rightarrow$ $\eta\sigma^{+-}$		0.027 $\pm$ 0.004		0.033	0.026
5 E(0 <sup>-+</sup> ) $\rightarrow$ $a_0^0\pi^0$		0.025 $\pm$ 0.004		0.025	0.028
E(0 <sup>-+</sup> ) $\rightarrow$ $a_0^\pm\pi^\mp$		0.035 $\pm$ 0.005		0.035	0.039
6 E(1 <sup>++</sup> ) $\rightarrow$ $\eta\sigma^0$			0.000	0.002	
E(1 <sup>++</sup> ) $\rightarrow$ $\eta\sigma^{+-}$			0.001	0.003	
7 E(1 <sup>++</sup> ) $\rightarrow$ $a_0^0\pi^0$			0.012	0.000	
E(1 <sup>++</sup> ) $\rightarrow$ $a_0^\pm\pi^\mp$			0.004	0.001	
20 $\eta X(1^{--})$ l=0	0.044	0.033 $\pm$ 0.004	0.007	0.101	0.023
$\eta X(1^{--})$ l=2	0.018	0.018 $\pm$ 0.003	0.007	0.022	0.013
21 X(1 <sup>--</sup> ) $\rightarrow$ $\eta\rho^0$	0.011	0.014 $\pm$ 0.003	0.008	0.009	0.013
22 $\eta'\rho^0$	0.020	0.022 $\pm$ 0.003	0.035	0.027	
23 X(1 <sup>+-</sup> ) $\rightarrow$ $\eta\rho^0$	0.196	0.182 $\pm$ 0.010	0.139	0.131	0.146
24 X(1 <sup>+-</sup> ) $\rightarrow$ $a_0\pi$		0.012 $\pm$ 0.003	0.007	0.008	0.011
25 $\rho^0(X(0^{-+}) \rightarrow \eta\sigma)$	0.030	0.026 $\pm$ 0.004	0.016	0.031	0.023
26 $\rho^0(X(0^{-+}) \rightarrow a_0\pi)$	0.111	0.068 $\pm$ 0.006	0.050	0.056	0.053

because fit A, in the absence of a E/ $\iota$  contribution pulls the background too high.

Figure 5.3 shows the  $\pi\pi\eta$  invariant mass distributions with fit B. One sees that the peak region of the E/ $\iota$  is well described. Different parametrizations of the “background“ were made and showed that the results on E/ $\iota$  are insensitive to changes to the background (see 5.2.3). The total intensity required for a  $0^{-+}$  E/ $\iota$  particle is  $11.1 \pm 0.8\%$ , where the error is statistical only.

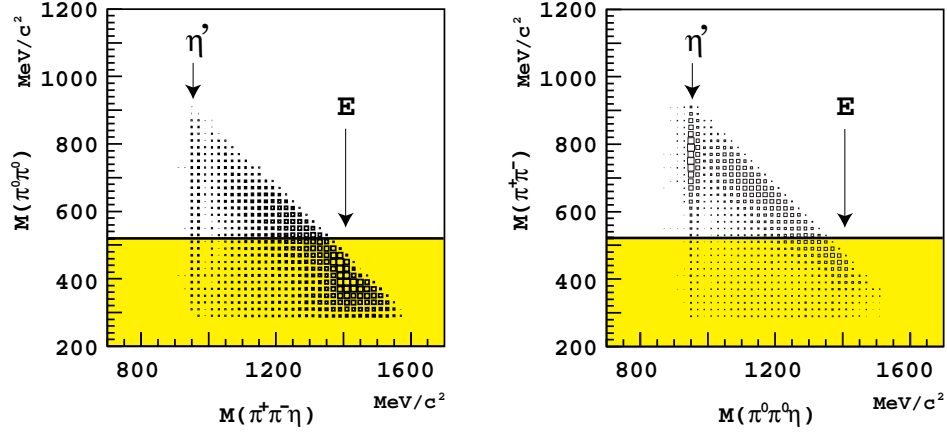


Figure 5.1: Scatterplot of the  $\pi\pi\eta$  invariant mass versus the recoiling  $\pi\pi$  invariant mass for data.

Assuming the same decays with  $E/\iota(1^{++})$  (chain 6,7) instead of  $E/\iota(0^{-+})$  I found a reduction of 1444 compared to fit  $A$ . The intensities are listed in table 5.2, hypothesis  $C$ . Fit  $C$  is however much worse than fit  $B$  ( $\Delta S = 1444$  compared to

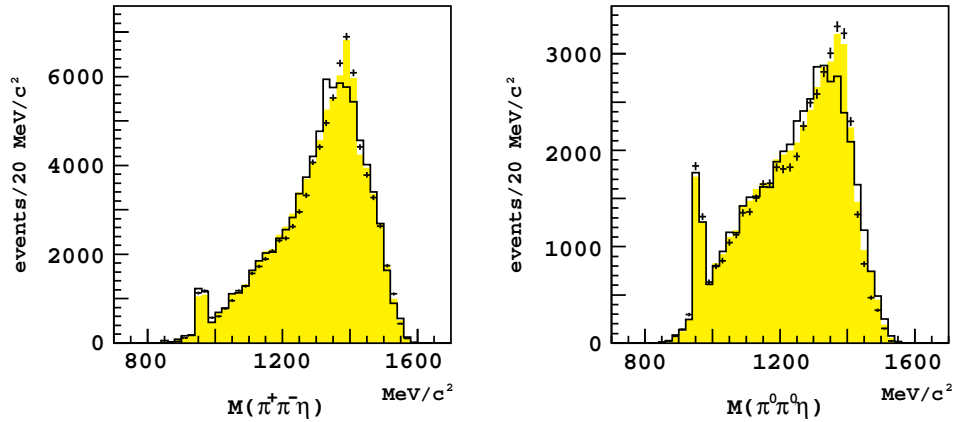


Figure 5.2:  $\pi\pi\eta$  invariant mass projection of the shaded region of fig 5.1 (e.g.  $M(\pi\pi) < 520$  MeV). The shaded region is the fit  $B$  with  $E/\iota(0^{-+})$  the line represents fit  $A$  without  $E/\iota$  (see text). The data are shown with error bars.

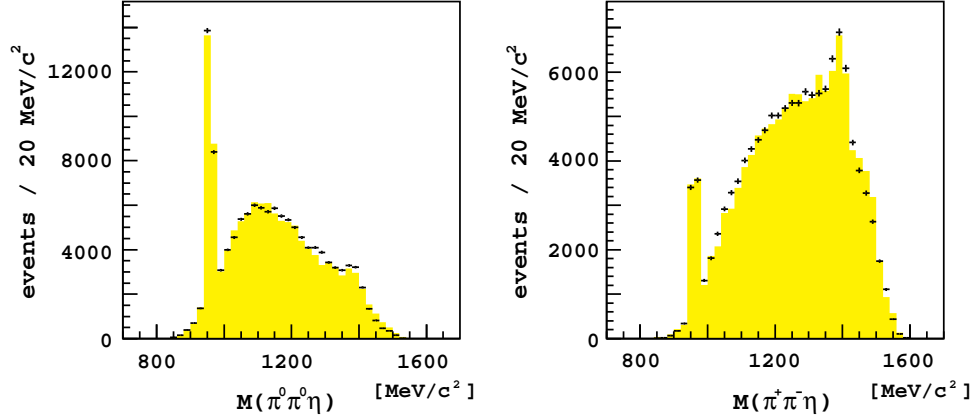


Figure 5.3:  $\pi\pi\eta$  invariant mass of all events used in fit  $B$  (shaded region). The data are shown with error bars.

$\Delta S = 8109!$ ). Fit  $C$  depends somewhat on the  $E/\iota$  mass and width, but the total intensity for the  $1^{++}$  contribution is never larger than 1.9%. There is only a broad minimum at a mass of approximately 1410  $\text{MeV}/c^2$  for which it was not possible to determine the width. If one introduces the  $E/\iota(1^{++})$  in addition to fit  $B$ , assuming that two states contribute to  $E/\iota$ , the likelihood decreases only by 139 and the  $E/\iota(1^{++})$  had a total intensity of  $0.6\% \pm 0.1\%$  (see table 5.2). Varying some background channels I found  $1^{++}$  contributions between 0.2 and 0.8%. This led to a  $1^{++}$  contribution of  $0.6\% \pm 0.4\%$  compatible with 0.

This means that the fit accepted the  $0^{-+}$  resonance and rejected the  $1^{++}$  state. The main reason is seen by comparing the angular distributions of a  $1^{++}$  and a  $0^{-+}$  state <sup>1</sup>. In order to get the  $E/\iota$  signal as clean as possible I selected events with a  $\pi\pi\eta$  invariant mass between 1367 and 1447  $\text{MeV}$ , I removed events where the recoiling  $\pi\pi$  invariant mass is larger than 520  $\text{MeV}$ , and I removed all  $\eta'$  events with a  $\pi\pi\eta$  invariant mass between 933 and 983  $\text{MeV}$ . Figure 5.4 shows the angular distributions for fit  $B$  in figure a) and b). If one replaces the  $0^{-+}$  with a  $1^{++}$  contribution, using the amplitudes of fit  $B$ , one finds pictures c) and d) which clearly disagree with the data.

The intensities given in table 5.2 for the different  $E/\iota(0^{-+})$  decays show an important  $E/\iota \rightarrow a_0\pi$  contribution. In order to prove that these  $a_0$  events are real, I used all events for which the  $\pi\pi\eta$  mass lies inside a window of 1367-1447

<sup>1</sup>In the absence of background and interferences a  $0^{-+}$  decays isotropically to  $0^{++}$  and  $0^{-+}$  while a  $1^{++}$  state decays as  $\sim \cos^2\theta$ .

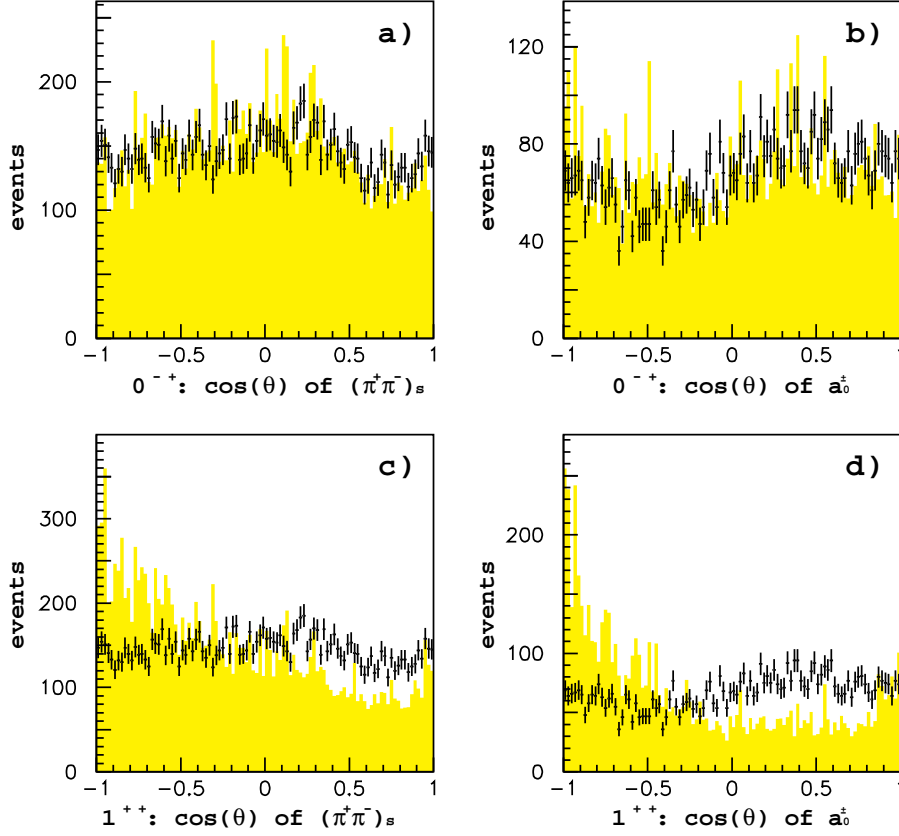


Figure 5.4: Angular distributions of the  $(\pi^+\pi^-)_s$  (a) or  $a_0^\pm$  (b) in the restframe of the  $E/\iota$  ( $\rightarrow \pi^+\pi^-\eta$ ) with respect to the flight direction of the  $E/\iota$  in the laboratory. Grey: fit for  $0^{-+}$ . The bottom figures c) and d) show the predictions when the  $0^{-+}$  is replaced by a  $1^{++}$  of the same intensity. The data are shown with error bars.

MeV ( $E/\iota$  region) and plotted the  $\eta\pi$  invariant mass (figure 5.5). A strong  $a_0$  peak is observed, and the fit describes the data reasonably well. The fit using the  $1^{++}$  hypothesis (fit  $C$ ) is shown in the upper insets. It is clearly much worse than fit  $B$ . The histogram of the  $\pi\eta$  invariant mass for events which have a  $\pi\pi\eta$  invariant mass in the side bins of the  $E/\iota$  (1327-1367, 1447-1487 MeV) was subtracted from the corresponding histogram with a  $\eta\pi\pi$  invariant mass in the  $E/\iota$  region (1367-1447 MeV). This is shown in the lower insets of figure 5.5. One

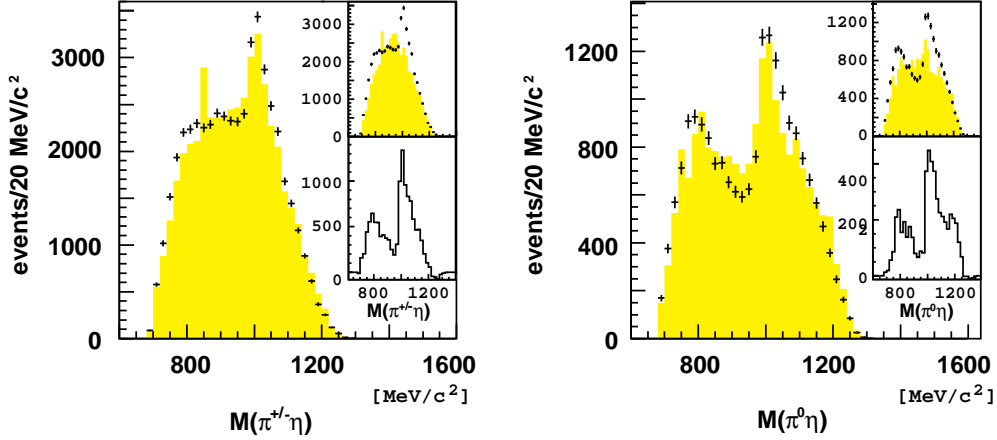


Figure 5.5:  $\pi\eta$  mass distributions for events which are located in the E region (e.g.  $1367 \text{ MeV} < M(\pi\pi\eta) < 1447 \text{ MeV}$ ) and which have a invariant mass of the recoiling  $\pi\pi$  system below  $520 \text{ MeV}/c^2$ . The shaded region is the fit using the  $0^{-+}$  hypothesis (fit  $B$ ). The upper insets show the fits for the  $1^{++}$  hypothesis instead. The lower insets show an  $E/\nu$  side-bin subtraction of the  $a_0$  region.

can estimate 2500-3000  $a_0^\pm$  and 1300-1700  $a_0^0$  events. This is in good agreement with the expected 4948 ( $a_0^\pm$ ) and 3171 ( $a_0^0$ ) events required by the fit  $B$  (table 5.2 with 126866 events) if one takes into account that  $\sim 50\%$  of the  $a_0$  events are lost by the mass windows in the side-bin subtraction.

To demonstrate that the  $E/\nu$  is well understood I also removed the events which have a  $\pi\pi\eta$  invariant mass in the  $\eta'$  window ( $958 \pm 25 \text{ MeV}$ ). This cut was applied to both data and Monte Carlo events after having fitted all  $\pi^+\pi^-\pi^0\pi^0\eta$  events (fit  $B$ ). As shown in figure 5.6 the description is very good. Fit  $E$  shows the results if one actually fits this reduced data set. Of course one cannot compare the likelihoods because data sizes are different. The intensities (which are normalized to 126866 events) agree for  $E/\nu$  with those of fit  $B$  within errors. This means that the interference between the decay chains of the  $E/\nu$  and the  $\eta'$  are small and that the results on  $E/\nu$  are independent from the fit results in the  $\eta'$  region.

One would actually expect that the decay  $\bar{p}p \rightarrow (\pi^+\pi^-)_s\eta', \eta' \rightarrow \pi^0\pi^0\eta$  would have the same intensity as  $\bar{p}p \rightarrow (\pi^0\pi^0)_s\eta', \eta' \rightarrow \pi^+\pi^-\eta$ . But fit  $B$  shows that the intensity of the former is a factor of 2 larger.

I will try to sketch a probable scenario. The reconstruction of our  $\pi^+\pi^-(\eta' \rightarrow \pi^0\pi^0\eta)$  is correct, because the systematical errors of the  $\pi^0$  and  $\eta$  decaying into  $2\gamma$

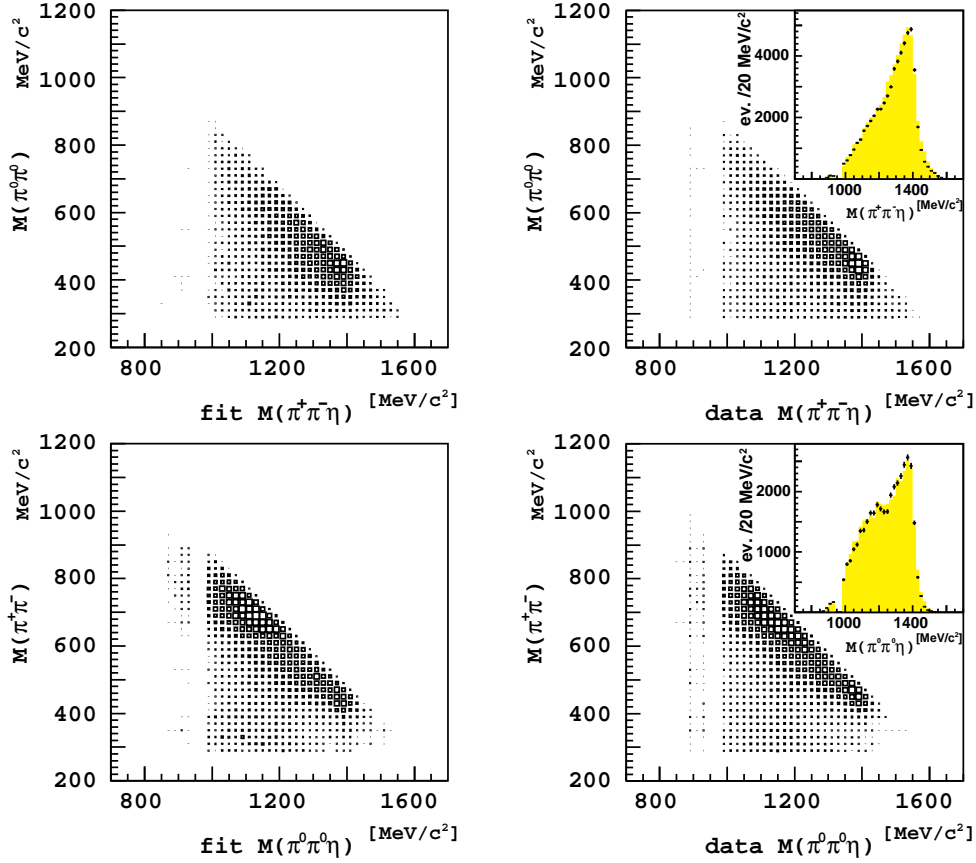


Figure 5.6: Scatterplots and mass projections (insets) when all  $\eta'$  events are removed from both data and fit  $B$ .

are well understood. The  $\eta'$  decay into  $\pi^+\pi^-\eta$  produces mostly charged  $\pi$  with a low transverse momentum. About half of the pions have a transverse momentum of less than 126 MeV/c in the laboratory. Their trajectories cross several sectors of the jet drift chamber. We know that the present reconstruction program has a low efficiency connecting such track segments to a long track. This effect is insufficiently modelled in the Monte Carlo program. Thus the  $\pi^0\pi^0\eta'$  channel gets an intensity which is too small.

There are therefore still some open question about the  $\eta' \rightarrow \pi^+\pi^-\eta$  in this data set. But this does not affect the study of the  $E/\iota$ . The data is well described by the fit. All fits find similar results, for the  $E/\iota$  intensities, even if one removes the  $\eta'$  (see tables 5.2 and 5.3).

Table 5.3: Mass and width for different background simulations.

change of hypothesis	mass MeV	error MeV	width MeV	error MeV	$\frac{E \rightarrow (\pi\pi)_s \eta}{E \rightarrow a_0 \pi}$	tot E intensity
best hypothesis $B$	1409	1	86	3.5	0.73	11.1%
inf. broad $1^{--} \rightarrow \rho'$	1409	1	88	4.0	0.78	13.9%
inf. broad $1^{+-} \rightarrow b_1$	1410	1	92	5.0	0.69	10.2%
adding $0^{-+}(1295)$	1407	1	82	3.5	0.75	11.0%
$\eta'$ Gauss $\rightarrow$ Breit-Wigner	1410	1	99	8.0	0.66	12.0%
$\eta'$ removed	1407	2	90	3.0	0.69	11.3%

Further tests were performed by including in fit  $B$  the additional chains given in table 5.1. These contributions did not affect significantly the result of fit  $B$ . The  $\eta(1295)$  with  $\Gamma=53$  MeV (chains 11, 12) was added and treated analogously to the  $E(0^{-+})$ . I found a reduction of the likelihood of 279. The  $a_2(1650)$  found by the Crystal Barrel [41] decaying via  $\pi\eta'$  (chain 8) led to a reduction  $\Delta S$  of 356. Replacing the  $X(0^{-+})\rho$  in chains 25, 26 by a  $E/\iota(0^{-+})\rho$  contribution (chains 27, 28) increased  $S$  by 1420 and moved the width of the  $E/\iota$  to unphysical high values.

Introducing a  $\rho'$  with a width of 320 MeV (chains 29, 30) instead of a direct  $1^{--}$  contribution (chains 20 and 21) resulted in an increase of  $S$  by 356. Replacing the direct contribution  ${}^3S_1 \rightarrow (\pi^0\pi^0)_s X(1^{+-})$  (chains 23 and 24) by  ${}^3S_1 \rightarrow (\pi^0\pi^0)_s b_1(1235)$  (chains 31 and 32)  $S$  increased by 3906. Replacing the  $X(0^{++})$  chains 1, 2 with the  $f_0(1365)$  found by the Crystal Barrel [30] (chains 9, 10) led to an increase of  $S$  by 5560. Mass and width of the  $\rho'$ ,  $b_1$  and  $f_0(1365)$  are not determined. They prefer to slide to larger values.

### 5.2.3 $E/\iota$ Mass and Width

To determine the mass and the width of the  $E/\iota$  I ran a large number of fits varying mass and width by hand. The log likelihood ( $S$ ) variations for the best fit  $B$  is shown in figure 5.7. The spline is minimal at 1409 MeV for the mass and at 86 MeV for the width.

The error on the mass and width are dominated by the systematics. To pin down the systematical error it is important to understand the influence of the background on mass and width of the  $E/\iota$ . I tried different background channels and ran for each hypothesis several fits with different masses and width of the  $E/\iota$  to determine the minimum of the likelihood. They are listed in table 5.3.

Using a Breit-Wigner instead of a Gaussian to describe the  $\eta'$  produced a

substantial worse fit,  $\Delta S$  increasing by 9012. The  $E/\iota$  mass and width remained close to the values of fit  $B$ . Because the description of the data by all these fits was clearly worse than for the best fit, I used them only to estimate the systematic error (including the error on energy calibration):

$$\begin{aligned} m(E/\iota) &= 1409 \pm 3 \text{ MeV} \\ \Gamma(E/\iota) &= 86 \pm 10 \text{ MeV} \end{aligned} \quad (5.19)$$

### 5.2.4 Branching Ratios

Using the intensities of fit  $B$  given in table 5.2 I find the following ratio of branching ratios for  $E/\iota$  decay into  $\pi\pi\eta$ :

$$\frac{B(E/\iota \rightarrow (\pi\pi)_s\eta)}{B(E/\iota \rightarrow \pi a_0, a_0 \rightarrow \eta\pi)} = 0.73 \pm 0.11 \pm 0.10 \quad (5.20)$$

where the first error is statistical and the second systematical. The systematical error is estimated from the variation in the ratio for different background channels (table 5.3). The total contributions of  $E/\iota$  to  $\pi^+\pi^-\pi^0\pi^0\eta$  is  $(11.1 \pm 0.8 \pm 1.8)10^{-2}$ .

The branching ratio for  $\bar{p}p \rightarrow \pi^+\pi^-\pi^0\pi^0\eta$  was estimated in section 4.4 and found to be  $2.08 \pm 0.34\%$ . Subtracting the contribution from  $\omega\eta\pi^0$  and  $\eta\eta\pi^0$

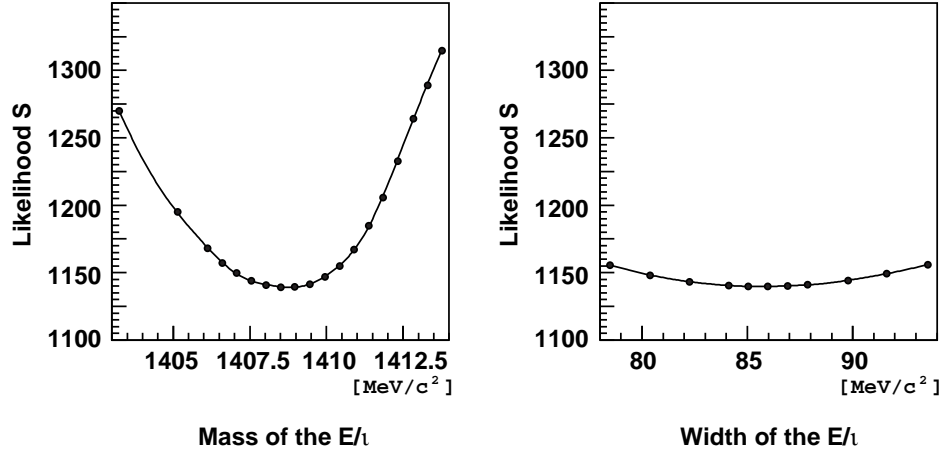


Figure 5.7: Result of several fits to the hypothesis  $B$  with different masses and widths. The variation of the mass was done with a width of 86 MeV and the variation of the width with a mass of 1409 MeV. The lines are spline fits.

table 4.3 to  $\pi^+\pi^-\pi^0\pi^0\eta$  ( $\omega \rightarrow \pi^+\pi^-\pi^0$ , and twice the branching ratio for  $\eta \rightarrow \pi^+\pi^-\pi^0$ ) one finds  $1.38 \pm 0.35\%$ . This leads to the absolute branching ratio

$$B[\bar{p}p \rightarrow \pi\pi(E/\iota \rightarrow \eta\pi\pi)] = (1.53 \pm 0.47)10^{-3} \quad (5.21)$$

From the 298'508  $\pi^+\pi^-\pi^0\pi^0\eta$  events the kinematic fit kept 126'866 events with a confidence level of less than 1% for the  $\omega\eta\pi^0$  or the  $\eta\eta\pi^0$  hypothesis. From the 303'200 kinematically fitted  $4\pi\eta$  Monte Carlo events the fit kept 187'284 events. I therefore get as a crosscheck

$$\begin{aligned} B[\bar{p}p \rightarrow \pi\pi(E/\iota \rightarrow \eta\pi\pi)] &= \\ B(\pi^+\pi^-\pi^0\pi^0\eta) \cdot \frac{126866}{298508} \cdot \frac{303200}{187284} \cdot 11.1\% &= (1.59 \pm 0.38)10^{-3}, \end{aligned} \quad (5.22)$$

which is in excellent agreement with equation (5.21).

The CERN-Collège de France group [1] found

$$\bar{p}p(^1S_0) \rightarrow (E \rightarrow K\bar{K})\pi\pi = (2.0 \pm 0.2)10^{-3} \quad (5.23)$$

They reported that 50% decays via  $K^*\bar{K}$  which implies that

$$\bar{p}p(^1S_0) \rightarrow \pi\pi E, E \rightarrow \pi(a_0 \rightarrow K\bar{K}) = (1.0 \pm 0.1)10^{-3}, \quad (5.24)$$

assuming that the non  $K^*\bar{K}$  contribution is  $a_0\pi$ . I find (table 5.2) that

$$\bar{p}p(^1S_0) \rightarrow (\pi\pi)_s E, E \rightarrow \pi(a_0 \rightarrow \eta\pi) = (0.88 \pm 0.22) \cdot 10^{-3}. \quad (5.25)$$

Therefore one can conclude that

$$\frac{a_0 \rightarrow K\bar{K}}{a_0 \rightarrow \eta\pi} = 1.14 \pm 0.31. \quad (5.26)$$

In the decay  $J/\Psi \rightarrow \gamma E/\iota, E/\iota \rightarrow a_0\pi$  the MARK III collaboration [9] reported a branching ratio for the decay of the  $a_0$  into  $K\bar{K}$  of  $(6.6_{-0.16}^{+0.17+0.24}) \cdot 10^{-4}$ . If the  $a_0$  decays into  $\pi^\pm\eta$ , they found  $(3.38 \pm 0.33 \pm 0.59)10^{-4}$  [18]. Taking into account the  $a_0$  decay into  $\pi^0\eta$  one gets:

$$\frac{a_0 \rightarrow K\bar{K}}{a_0 \rightarrow \eta\pi} = 1.30 \pm 0.28, \quad (5.27)$$

which is consistent with our result, equation (5.26).

It is also interesting to compare the MARK III  $a_0 \rightarrow \eta\pi$  data mentioned above with the DM 2 result [42] who measured the  $E/\iota$  decay to  $\eta\pi^+\pi^-$  in radiative  $J/\Psi$  decay. Using equation (5.20) together with the MARK III result one finds:

$$B(J/\Psi \rightarrow \gamma E/\iota \rightarrow \gamma\eta\pi^+\pi^-) = 1.73 \cdot (3.38 \pm 0.68)10^{-4} = (5.85 \pm 1.22)10^{-4} \quad (5.28)$$

which is in excellent agreement with  $(7.0 \pm 1.3)10^{-4}$  from [42].

From the fit and the data one can see that  $E/\iota$  decays into  $\pi^0\pi^0\eta$ . This implies that the  $E/\iota$  has isospin  $I=0$ . This is the first experiment which determines unambiguously that  $E$  observed in  $\bar{p}p$  annihilation is isoscalar and has  $C=1$ .

Comparing our  $\pi^+\pi^-\eta'$  with Asterix one finds that their absolute branching ratio  $\rho\eta'$  of  $(1.81 \pm 0.44)10^{-3}$  is in agreement with our value of  $(1.46 \pm 0.42)10^{-3}$ . Asterix finds also an absolute  $\pi^+\pi^-\eta'$  branching ratio of  $(3.46 \pm 0.67)10^{-3}$ , where our number is  $(6.04 \pm 1.60)10^{-3}$ .

### 5.3 Conclusion and outlook

The mass, width, quantum numbers and decay modes of the  $E$  observed in  $\bar{p}p$  annihilation are consistent with those of  $\eta(1420)/\iota$  observed in radiative  $J/\Psi$  decay. Hence  $E$  and  $\eta(1420)$  are indeed the same object.

As I pointed out in the motivations, one would like to know if the  $E/\iota$  particle is the excited  $\eta'$ . Indeed it could. It has the correct  $J^{PC}$  and lies in the expected mass region. But assuming that  $\pi(1300)$  and  $\eta(1295)$  are correctly identified as the first  $\pi$  and  $\eta$  radial excitations, one would expect ideal mixing. Using the Gell-Mann Okubo mass formula with the  $K(1460)$  one would expect the  $s\bar{s}$  member around 1600 MeV. There is a candidate found by the Mark III collaboration [9]: the  $0^{-+}(1490)$  decaying to  $K^*\bar{K}$ . It was confirmed by the Obelix collaboration [11], and lies closer to the expected 1600 MeV value.

The present measurement of the  $E/\iota$  particle is compatible with the  $E(1420)$  found by Baillon et al. and with the  $\iota$  found in  $J/\Psi$  decay. The latter is a gluon rich environment, so maybe the  $E/\iota$  is a glueball. The MIT bag model predicts a  $0^{-+}$  glueball at 1500 MeV. This would fit nicely. But it also predicts a  $0^{++}$  glueball at 1000 MeV where no glueball has been found so far. Lattice gauge theories [6] predict a  $0^{++}$  glueball at 1500 MeV, where the Crystal Barrel experiment found a strong candidate [5]. The corresponding  $0^{-+}$  is expected to be beyond 2000 MeV, but mixing with  $\bar{q}q$  can distort and reorder the glueball spectrum. For a primitive  $0^{-+}$  glueball (no mixing with quarks) one would expect the decay into  $(\pi\pi)_s\eta$ , which is observed in this experiment.

One should now go back and measure the  $E/\iota$  decay into  $K\bar{K}\pi$  with the Crystal Barrel, in order to study both the  $E/\iota$  and the  $0^{-+}(1490)$  with high

statistics, establishing the latter resonance and testing if it is really a good  $\bar{s}s$  candidate. It is also important to determine the decay branching ratio of the  $E/\iota$  into  $\bar{K}K\pi$  via  $K^*\bar{K}$  and  $a_0\pi$  with better accuracy.

The huge statistics and the small background contributions of other final states in this work warrant further investigations. In particular:

- It is clearly an approximation to fit the data in terms of Breit-Wigners. A description with the K-matrix formalism which preserves unitarity will allow to fit overlapping resonances in the same decay chain. It is also necessary to measure the  $\bar{K}K$  contribution to the K-matrix with the Crystal Barrel. This is the main task for the new silicon vertex detector, which will enable us to trigger on  $K_s \rightarrow \pi^+\pi^-$ .
- To study the  $E/\iota \rightarrow \bar{K}K\pi$  decay it would be important to measure a channel like  $K_s K_s \pi^0 \pi\pi$ . A combined trigger for both measurements should be possible.
- The present fit could be repeated with the  $\pi\eta\omega$  events included using the information from the spin parity analysis done in the  $\pi^0\eta\omega, \omega \rightarrow \pi^0\gamma$  final state [28]. This needs a computer with at least 512 Mbyte physical memory and a fast CPU. In addition it may be necessary to optimize the fit routine itself (Minuit) in order to obtain reasonable calculation times.

# Bibliography

- [1] P. Baillon et al., *Nuovo Cimento* **50A** (1967) 393
- [2] C. Amsler and F. Myhrer *Ann. Rev. Nucl. Part. Sci.* **41** (1991) 219
- [3] J. Weinstein and N. Isgur, *Phys. Rev. Lett.* **48** (1982) 659
- [4] J. Weinstein and N. Isgur, *Phys. Rev.* **D27** (1983) 588
- [5] C. Amsler and F. E. Close, *in preparation*
- [6] C. Amsler, *Proc. Int. HEP Conference, Glasgow* (1994)
- [7] K. Duch et al., *Z. Phys.* **45** (1989) 223
- [8] J.-E. Augustin et al., *Phys. Rev* **D46** (1992) 1951
- [9] Z. Bai et al., *Phys. Rev. Lett.* **65** (1990) 2507
- [10] Review of Particle Properties *Phys. Rev.* **D50** (1994) 1180
- [11] A. Masoni et al., *Proc. LEAP 94 Conf., Bled, Slovenia* (1994)
- [12] D.L. Scharre et al., *Phys. Lett.* **97B** (1980) 329
- [13] S.U. Chung et al., *Phys. Rev. Lett.* **55** (1985) 779
- [14] A. Ando et al., *Phys. Rev. Lett.* **57** (1986) 1296
- [15] J. Becker et al., *Phys. Rev. Lett.* **59** (1987) 186
- [16] H.J. Behrend et al., *Z. Phys.* **C42** (1989) 367
- [17] T.A. Armstrong et al., *Z. Phys.* **56** (1992) 29
- [18] M. Burchell, *Nucl. Phys.* **B21** (suppl.) (1991) 132

- [19] E. Aker et al., *CERN/PSCC/85-86, PSCC P90* (1985).
- [20] E. Aker et al., *Nucl. Instr.* **A321** (1992) 69
- [21] D. Urner, Diploma, *Universität Zürich* (1989), unpublished.
- [22] F. Krenrich, Diploma, *Ludwig-Maximilians-Universität München* (1991), unpublished.
- [23] R. Veenhof, *CERN program library, W5050* (1989)
- [24] R. Brun, J. Zoll, *CERN program library, Q100* (1987)
- [25] R. Brun et al., *CERN Report DD/EE/84-1* (1987)
- [26] H.C. Fesefeld, *PYTHIA Report, 85-02, RWTH Aachen* (1985)
- [27] C. Amsler et al. *Phys. Let.* **B327** (1994) 425
- [28] S. Ravndal: *PhD thesis Universität Bochum* (1993), unpublished
- [29] C. Amsler et al. *Phys. Letters* **B291** (1992) 347
- [30] C. Amsler et al. *Phys. Letters* **B322** (1993) 431
- [31] P. Weidenauer et al. *Z. Phys.* **C47** (1990) 353
- [32] C. Amsler et al., *Phys. Let. B* (1994) 259
- [33] M. Jacob and G. C. Wick, *Ann. Phys. (NY)* **7** (1959) 401
- [34] D. Herndon, P. Söding and R. J. Cashmore, *Phys. Rev.* **D 11** (1975) 3165
- [35] C. Amsler and J. C. Bizot, *Comp. Phys. Com.* **30** (1983) 21
- [36] F. v. Hippel and C. Quigg, *Phys. Rev.* **D5** (1972) 624
- [37] M. Locher, private communication
- [38] K. L. Au et al., *Phys. Rev.* **D35** (1987) 1633
- [39] G. Reifenröther and E. Klempt, *Phys. Lett.* **B245** (1990) 129
- [40] D. Alde et al., *Phys. Rev.* **B177** (1986) 115
- [41] C. Amsler *Phys. Lett.* **B333** (1994) 277
- [42] J.-E. Augustin et al., *Phys. Rev.* **D42** (1990) 10

# Acknowledgements

In particle physics the experiments like the Crystal Barrel are performed by a large number of physicists. The success of an experiment depends on a good teamwork between all members of the collaboration. This was fulfilled very nicely with the Crystal Barrel team, and I would like to thank everybody for the help, cooperation and support. In particular I would like to thank:

Professor Claude Amsler, my advisor, who supported my work patiently with a lot of ideas and constructive criticism. With his experience and his persistence, he was an important help in overcoming problems.

Brigitt Schmid for various discussions and ideas.

Curtis Meyer who was a remarkable source of knowledge in respect to physics and informatics.

Toni Noble who helped a lot by undertaking the responsibility about the PWC when I was not at CERN.

Dieter Walther who was always willing to help, if I had to solve a hardware problem.

Nigel Hessey for his excellent work and his help with the software trigger.

Michael Doser and Christian Völcker for their work as software coordinators and their help with the reconstruction of the data.

Sven Dombrowski, Stefan Spanier and Farid Ould-Saada for a lot of fruitful discussions and for their patience to debate again and again about the details of a spin-parity analysis.

Hanspeter Beck and Christian Dollfus, who helped patiently with my daily small (but urgent) problems in physics, mathematics and informatics.

Stefan Dangel and Stefan Schafroth for their English support.

The people of the workshop of the Physik-Institut, who always found the time to bring my ideas to reality, yesterday!